

Highly resolved mapping of NO₂ vertical column densities from GeoTASO measurements over a megacity and industrial area during the KORUS-AQ campaign

Gyo-Hwang Choo¹, Kyunghwa Lee¹, Hyunkee Hong^{1*}, Ukkyo Jeong^{2,3}, Wonei Choi⁴, Scott J. Janz³

¹Environmental Satellite Center, National Institute of Environmental Research, Hwangyeong-ro 42, Seo-gu, Incheon, Republic of Korea, 22689

²Earth System Science Interdisciplinary Center, University of Maryland, College Park, Maryland, USA 20740

³NASA Goddard Space Flight Center, Greenbelt, Maryland, USA, 20771

⁴Division of Earth Environmental System Science, Major of Spatial Information Engineering, Pukyong National University, Busan 48513, South Korea

Correspondence to: Hyunkee Hong; Tel: +82 32 560 8437; Fax: +82 32 560 8460; E-mail address: wanju77@korea.kr

Abstract. The Korea-United States Air Quality (KORUS-AQ) campaign is a joint study between the United States National Aeronautics and Space Administration (NASA) and the South Korea National Institute of Environmental Research (NIER) to monitor megacity and transboundary air pollution around the Korean Peninsula using airborne and ground-based measurements. Here, tropospheric nitrogen dioxide (NO₂) slant column density (SCD) measurements were retrieved from Geostationary Trace and Aerosol Sensor Optimization (GeoTASO) L1B data during the KORUS-AQ campaign (May 2 to June 10, 2016). The retrieved SCDs were converted to tropospheric vertical column densities using the air mass factor (AMF) obtained from a radiative transfer calculation with trace gas profiles and aerosol property inputs simulated with the Community Multiscale Air Quality (CMAQ) model and surface reflectance data obtained from the Moderate Resolution Imaging Spectroradiometer (MODIS). For the first time, we examine highly resolved (250 m × 250 m resolution) tropospheric NO₂ over the Seoul and Busan metropolitan regions, and the industrial regions of Anmyeon. We reveal that the maximum NO₂ VCDs were 4.94×10^{16} and 1.46×10^{17} molecules cm⁻² at 9 AM and 3 PM over Seoul, respectively, 6.86×10^{16} and 4.89×10^{16} molecules cm⁻² in the morning and afternoon over Busan, respectively, and 1.64×10^{16} molecules cm⁻² over Anmyeon. The VCDs retrieved from the GeoTASO airborne instrument were correlated with those obtained from the Ozone Monitoring Instrument (OMI) ($r = 0.48$), NASA's Pandora Spectrometer System ($r = 0.91$), and NO₂ mixing ratios obtained from in situ measurements ($r = 0.07$ in the morning, $r = 0.26$ in the afternoon over the Seoul, and $r > 0.56$ over Busan). Based on our results, GeoTASO is useful for identifying NO₂ hotspots and their spatial distribution in highly populated cities and industrial areas.

1 Introduction

Nitrogen dioxide (NO₂) is one of the most important atmospheric trace gases and plays a key role in aerosol production and tropospheric ozone photochemistry (Boersma et al., 2004; Richter et al., 2005). Furthermore, high concentrations of NO₂ in the atmosphere have adverse effects on human health, such as respiratory infections, and associated symptoms (Brauer et al., 2002; Latza et al., 2009).

The main sources of NO₂ in the atmosphere are fossil fuel combustion from vehicles and thermal power plants, lightning, and biogenic soil processes. Furthermore, NO₂ concentrations are highly correlated with population size (Lamsal et al., 2013). The implementation of emission control technology and environmental regulation has led to a decrease in surface NO₂ concentrations in Western Europe, the United States, and Japan in the last few decades (Richter et al., 2005). The concentration of NO₂ in major metropolitan cities in South Korea and China is over 3 times larger than over similarly sized cities in Europe and United States, despite NO₂ concentration decreasing in China and South Korea (de Foy et al., 2016; Choo et al., 2020).

To date, several low-orbit space borne sensors, such as the Global Ozone Monitoring Experiment (GOME) (Burrows et al., 1999), the Scanning Imaging Spectrometer for Atmospheric Cartography (SCIAMACHY) (Burrows et al., 1995), the Ozone

Monitoring Instrument (OMI) (Levelt et al., 2006), the GOME-2 (Callies et al., 2000), and the Tropospheric Monitoring Instrument (TROPOMI) (Veefkind et al., 2012), have monitored atmospheric ozone and its precursors including NO₂ and formaldehyde (HCHO) as a proxy for volatile organic compounds (VOCs). Furthermore, the Geostationary Environment Monitoring Spectrometer (GEMS) (Choi et al., 2018; Kim et al., 2020), which was launched on February 18, 2020, will form a constellation of geostationary satellites including the upcoming Tropospheric Emission: Monitoring of Pollution (TEMPO) (Zoogman et al., 2017) and Sentinel-4 platforms, to continuously observe the air quality of the Northern Hemisphere during the day.

NO₂ retrievals from space borne hyperspectral measurements are typically conducted using the differential optical absorption spectroscopy (DOAS) method (Platt and Stutz, 2008) to first retrieve the view-dependent slant column density (SCD), and then radiative transfer models are used to determine the vertical column density (VCD) using an air mass factor (AMF) correction. Previous and ongoing space borne instruments use various radiative transfer codes and model input assumptions to calculate NO₂ AMF values at coarse spatial resolution. Because AMF weighting has a large impact on NO₂ retrievals using the DOAS method, it is important to use model input assumptions that most accurately match viewing and atmospheric conditions. Several studies have demonstrated the sensitivity of AMF calculations to inaccurate model input parameters (e.g., *a priori* NO₂ vertical profile and aerosol properties) and *a priori* data (cloud information and surface reflectance) (Leitão et al., 2010; Hong et al., 2017; Lorente et al., 2017; Boersma et al., 2018). NO₂ retrievals have also been consistently conducted based on surface remote sensing measurements including the Multi-Axis DOAS (MAX-DOAS), Système D'Analyse par Observations Zénithales (SAOZ) spectrometer (Pastel et al., 2014), and Pandora (Herman et al., 2009) systems. These ground-based measurements can be used as validation references for both airborne and space borne measurements.

NO₂ retrievals from airborne remote sensing instruments, such as the Geostationary Coast and Air Pollution Event (GEOCAPE) Airborne Simulator (GCAS) (Kowalewski and Janz, 2014), the Heidelberg Airborne Imaging DOAS Instrument (HAIDI) (General et al., 2014), the Geostationary Trace gas and Aerosol Sensor Optimization (GeoTASO) (Leitch et al., 2014), the Airborne Prism Experiment (APEX; Popp et al., 2012), the Airborne Imaging DOAS instrument for Measurements of Atmospheric Pollution (AirMAP; Meier et al., 2017; Schönhardt et al., 2015), the Small Whiskbroom Imager for atmospheric compositionN monitorinG (SWING; Merlaud et al. 2018), and the Spectrolite Breadboard Instrument (SBI; Vlemmix et al., 2017; Tack et al., 2019) have also been performed to identify local emission sources and obtain highly resolved horizontal NO₂ distributions.

Observations using airborne measurements have an advantage as they enable the observation of horizontal distributions of trace gases at resolutions higher than those of space-based satellites and provide data over a wider area than those of ground-based observations. For example, Nowlan et al. (2018) retrieved tropospheric NO₂ VCDs over Houston, Texas, during the Deriving Information on Surface Conditions from Column and Vertically Resolved Observations Relevant to Air Quality (DISCOVER-AQ) campaign and identified a high correlation with data retrieved from Pandora. Popp et al. (2012) also presented the morning and afternoon NO₂ spatial distribution in Zurich, Switzerland, using APEX. Tack et al. (2017) have conducted high-resolution mapping of NO₂ over three Belgium cities (Antwerp, Brussels, and Liège) using APEX and Judd et al. (2020) and Tack et al. (2021) compared NO₂ VCDs retrieved from GCAS/GeoTASO and APEX with those obtained from TROPOMI over New York City and Antwerp and Brussels, respectively. Merlaud et al. (2013) observed NO₂ VCDs in Turceni over Romania using SWING mounted on an unmanned aerial vehicle (UAV) during the Airborne Romanian Measurements of Aerosols and Trace gases (AROMAT) campaign. These existing NO₂ retrievals, using airborne measurements, have been useful in constraining regional air quality models due to the highly resolved source identification and the ability to tie these results to ground-based observations.

This work focuses on airborne NO₂ retrievals from GeoTASO. This instrument was developed by Ball Aerospace to reduce mission risk for UV-VIS air quality measurements from geostationary orbit for the GEMS and TEMPO missions (Leitch et al., 2014). The retrieval of NO₂, SO₂, and HCHO observed from GeoTASO L1B data using DOAS and principal component

analysis (PCA) (Wold et al., 1987) was conducted through the DISCOVER-AQ and KOREa-United States Air Quality (KORUS-AQ) campaigns (Nowlan et al., 2016; Judd et al., 2018; Choi et al., 2020; Chong et al., 2020). The KORUS-AQ campaign is a joint study between the National Institute of Environmental Research (NIER) and National Aeronautics and Space Administration (NASA) to monitor megacity air pollution and transboundary pollution, and to prepare for geostationary satellite (i.e., GEMS, TEMPO, and Sentinel-4) air quality observability (of trace gases and aerosols), organized from May to June 2016.

Although surface NO₂ concentrations in South Korea are the high due to high population density, high traffic volumes, and many industrial complexes and thermal power plants, and although NO₂ retrieval studies using airborne and ground measurements in North America, Europe, China, and Japan, data for South Korea remain limited. The specific objectives of this study are as follows:

- (1) To retrieve tropospheric NO₂ vertical column data using GeoTASO measurements over polluted regions of the Seoul and Busan metropolitan areas and the Anmyeon industrial regions of the Korean Peninsula.
- (2) To estimate NO₂ VCD uncertainties using error propagation accounting for spectral fitting errors and AMF uncertainties associated with input data errors, including aerosol optical depth (AOD), single scattering albedo (SSA), aerosol peak height (APH), and surface reflectance (SR).
- (3) To compare NO₂ VCDs retrieved from GeoTASO and those obtained from OMI and ground-based Pandora instruments, as well as surface in situ measurements.

2 KORUS-AQ campaign area, measurements, and model simulation

2.1 Campaign area

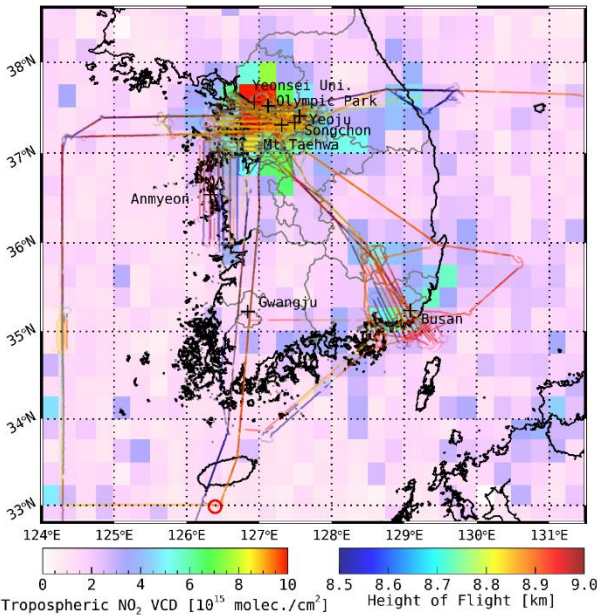


Figure 1. Flight paths of the NASA LaRC B200 aircraft carrying GeoTASO and the average tropospheric NO₂ VCDs obtained from OMI gridded to a 0.25° × 0.25° horizontal grid during the KORUS-AQ campaign period. The line color represents flight height. In this period, the GeoTASO observations focused on megacities (Seoul and Busan) and industrial complex area (Anmyeon) with high tropospheric NO₂ concentrations. The reference spectrum for spectral fitting is obtained from the radiation data over the Jeju Island (marked with red circle).

The Korean Peninsula, located on the Asia-Pacific coast, has a complex atmospheric environment by local emissions and long-range transport under appropriate weather conditions (Jeong et al., 2017; NIER and NASA, 2020; Choo et al., 2021). Seoul, the capital of South Korea, and the metropolitan area are densely populated, and power plants and industrial activities on the

113 northwest coast are conducted, which emit relatively large amounts of pollutants. The KORUS-AQ campaign conducted three-
114 dimensional observations, including ground-based remote, aircraft, satellite observation, and air quality modeling, to
115 understand the complex air quality and interpret the observations of GEMS launched in 2020. The KORUS-AQ campaign
116 period was from May 2 to June 10, 2016. During the KORUS-AQ campaign, air pollutants were conducted using the GeoTASO
117 on board the NASA Langley Research Center B200 aircraft to monitor air quality and long-range transport of pollutants over
118 the Korean Peninsula (NIER and NASA, 2020). The GeoTASO observations were conducted 30 times in 23 d out of 40 d.
119 Most observations were made once or twice a day. Each flight was planned and conducted on a day when the weather
120 conditions were fine and flight hours were approximately 2–4 h. We show the average values of GeoTASO flight information
121 such as flight time, altitude, speed, solar zenith angle (SZA), and viewing zenith angle (VZA) for the dates retrieved for NO₂
122 VCD, aerosol properties (AOD, SSA) extracted from CMAQ, and cloud fraction and SR extracted from the Moderate
123 Resolution Imaging Spectroradiometer (MODIS) in Table 1. Flight information on the date of aircraft observation can be found
124 at http://www-air.larc.nasa.gov/missions/korus-aq/docs/KORUS-AQ_Flight_Summaries_ID122.pdf. Figure 1 indicates the
125 flight routes of B200 and the tropospheric NO₂ VCD obtained from the OMI during the campaign period. The observations
126 were concentrated in the metropolitan areas of Seoul and Busan and the industrial areas of Anmyeon, with an average flight
127 altitude of ~8.5 km during KORUS-AQ.

128

129 **Table 1. Summary of information on the dates when NO₂ VCD was retrieved during the KORUS-AQ period (LT = UTC + 9**
130 **h). The average values of GeoTASO data sets for flight characteristics, aerosol properties, geometric information and cloud**
131 **information.**

Date	Jun 5	Jun 9 AM	Jun 9 PM	Jun 10 AM	Jun 10 PM
ROI	Anmyeon	Seoul metropolitan		Busan metropolitan	
Flight time (LT)	13:11–17:20	7:48–12:00	13:46–17:52	8:02–11:38	13:05–15:19
Flight altitude (km)	8.6	8.4	8.5	8.6	8.5
Flight speed (km hr ⁻¹)	117.0	116.2	117.6	117.2	117.1
SZA (°)	39.2	36.1	45.3	35.9	33.0
VZA (°)	11.9	12.6	12.8	12.1	11.8
AOD	0.27	0.40	0.21	0.13	0.09
SSA	0.966	0.980	0.949	0.981	0.968
Surface reflectance	0.07	0.09	0.09	0.06	0.06

132

133 As shown in Fig. 1, GeoTASO observations were conducted focusing on highly NO₂-polluted regions in the Seoul and Busan
 134 metropolitan areas and the Anmyeon region during the KORUS-AQ campaign. The Seoul metropolitan area (Seoul Special
 135 City, Gyeonggi Province, and Incheon City) is one of the most densely populated areas worldwide, with a population of
 136 approximately 20 million in 2016. Busan is the second-largest city in South Korea, with a population of approximately 3.4
 137 million in 2016. Anmyeon is located southwest of Seoul, with petrochemical complexes, steel mills, and thermal power stations
 138 in this area. The background color in Fig. 1 represents the average NO₂ VCD obtained from the OMI during the KORUS-AQ
 139 campaign period, showing over 1×10^{16} molecules cm⁻² over the Seoul metropolitan area. The OMI data were obtained with
 140 the Level 2.0 OMNO2 version 3.0 and downloaded from the NASA Earthdata search (<http://search.earthdata.nasa.gov/search/>).
 141 We calculated the arithmetic means of tropospheric NO₂ VCDs, like Choo et al. (2020), to obtain the grid data (0.25° × 0.25°)
 142 during the KORUS-AQ period. The average tropospheric NO₂ VCD data were excluded from May 30 2016 to Jun 9 2016,
 143 when the OMI data did not exist during the campaign period.

144 2.2 Pandora

145 NO₂ VCDs retrieved from the GeoTASO were validated using those from NASA's Pandora Spectrometer system. The Pandora
 146 spectrometer is a hyper-spectrometer that can provide direct sun measurements of UV-Vis spectra (280–525 nm with a full
 147 width at half maximum (FWHM) of 0.6 nm) for observing atmospheric trace gases. During the KORUS-AQ, eight Pandora
 148 instruments monitored NO₂ and ozone (O₃) VCD as depicted by plus symbols in Fig. 1. The retrieved data are available on the
 149 KORUS-AQ pages of NASA's Goddard Space Flight Center website
 150 (<https://avdc.gsfc.nasa.gov/pub/DSCOVER/Pandora/DATA/KORUS-AQ/>). We compared NO₂ VCDs obtained from five
 151 Pandora measurements (Busan university: 35.24 °N, 129.08 °E; Olympic park: 37.52 °N, 127.13 °E; Songchon: 37.41 °N,
 152 127.56 °E; Yeosu: 37.34 °N, 127.49 °E; Yonsei University: 37.56 °N, 126.93 °E) within 0.05° and 30 min with those from
 153 GeoTASO. Because NO₂ has a short atmospheric lifetime, especially during the summer (Shah et al., 2020), its spatial and
 154 temporal distributions vary notably. A detailed description of Pandora's operation during the KORUS-AQ campaign has
 155 previously been reported (Herman et al., 2018; Spinei et al., 2018).

156 2.3 Ground-based in situ NO₂ measurement

157 Although the basic physical quantity of VCD and the surface mixing ratio from in situ measurements are different, comparison
 158 of their spatiotemporal variations provides useful information for deriving surface air quality from airborne instruments (e. g.,
 159 Jeong and Hong, 2021a; 2021b). In this study, we compare the NO₂ VCDs (molecules cm⁻²) retrieved from GeoTASO to
 160 surface mixing ratios measured by ground-based in-situ monitoring network over South Korea (i.e., Air-Korea, a national real-
 161 time air quality network; <https://www.airkorea.or.kr/>). The instruments use the chemiluminescence method (Kley and
 162 McFarland, 1980), and approximately 400 air quality monitoring sites in Korea are registered in the system, providing hourly
 163 surface NO₂ concentrations. We compared NO₂ VCDs retrieved from GeoTASO within 0.5 km and 30 min with NO₂
 164 concentrations obtained from Air-Korea.

165 2.4 GeoTASO measurements

166 NO₂ VCDs were retrieved from the L1B radiance dataset (version: V02y) obtained using GeoTASO during the KORUS-AQ
 167 campaign. The NASA Goddard Space Flight Center conducted the L1B radiance calibration, which included offset and smear
 168 correction, gain matching, amplifier cross-talk correction, dark rate correction, integration normalization, sensitivity derivation,

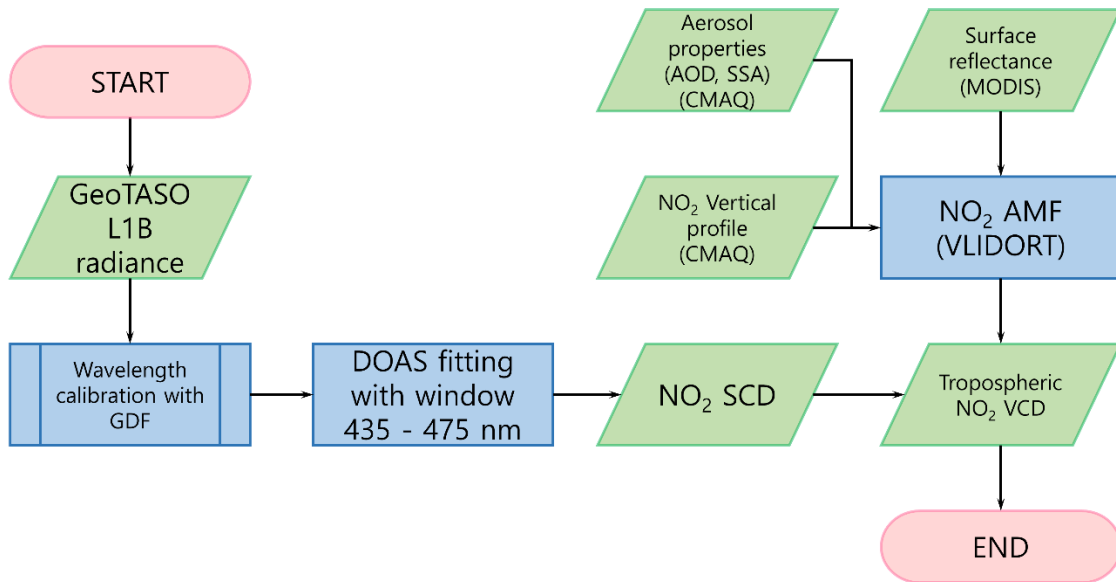
169 wavelength registration, geo-registration, non-linearity correction, and ground pixel geolocation (Kowalewski et al., 2017;
 170 Chong et al., 2020). The detailed specifications of GeoTASO are listed in Table 2 (Nowlan et al., 2016).

171

172 **Table 2. Summary of the GeoTASO instrument and optical specification.**

L1B version	V02y
Full cross-track field of view	45°
Single-pixel cross-track field of view	0.046°
Wavelength	UV: 290–400 nm
	VIS: 415–695 nm
Spectral resolution	UV: ~0.39 nm
(full width at half maximum, FWHM)	VIS: ~0.88 nm
CCD	1,056 (wavelength) × 1,033 (cross-track)
Spatial resolution before binning	~35 m (along-track) × 7 m (cross-track)
Spatial resolution after binning	~250 m (along-track) × 250 m (cross-track)

173



174

175 **Figure 2. Flowchart of the algorithm for retrieving tropospheric NO₂ data from GeoTASO.**

176

177 2.4.1 NO₂ slant column density retrieval

178 Figure 2 indicates the flowchart for retrieving the tropospheric NO₂ VCD from the GeoTASO. We first retrieved NO₂ SCDs
 179 using the DOAS method (Platt, 1994). Nonlinear least square minimization was used to retrieve the NO₂ SCDs which
 180 minimizes the difference between the measured optical depth and the modeled value in QDOAS software (Eq. (1); Danckaert
 181 et al., 2012).

$$182 \frac{\ln I(\lambda)}{\ln I_0(\lambda)} = -(\sum_{j=1}^m \rho_j \times \sigma'_j(\lambda) + B(\lambda) + R(\lambda) + A(\lambda) + N(\lambda)), \quad (1)$$

183

Where $I(\lambda)$ is the measured earthshine radiance at wavelength λ ; I_0 is the reference radiance from the reference sector (southern ocean of the Jeju Island denoted as the red circle in Fig. 1; 32.983°N, 126.392°E) at 9 AM on May 1 2016. The Community Multiscale Air Quality (CMAQ) modeling system data indicated that the NO_2 VCD from the surface to 50 hPa over this reference sector on this day was 6.75×10^{15} molecules cm^{-2} , and the mean of total NO_2 VCD obtained from the OMI during the KOURS-AQ period was 4.77×10^{15} molecules cm^{-2} with a standard deviation of 1.33×10^{15} molecules cm^{-2} . We also confirmed the stability of NO_2 distribution over this area using the TROPOMI offline data from 2019 to 2020. In this period, the NO_2 VCD from the TROPOMI was 4.81×10^{15} molecules cm^{-2} with a standard deviation of 0.43×10^{15} molecules cm^{-2} . The NO_2 VCD used as a reference sector obtained from CMAQ was mainly dominated by stratospheric NO_2 VCD. However, stratospheric NO_2 VCD has a relatively lower than tropospheric NO_2 VCD. The p_j represents the SCD of each species j ; $\sigma_j(\lambda)$ represents the differential gas phase absorption cross-section convolved with the Gaussian distribution function (GDF) with GeoTASO FWHM (the UV and VIS range were 0.34–0.49 nm and 0.70–1.00 nm, respectively (Nowlan et al., 2016)) at wavelength λ of species j , respectively.

We used the measured radiances at the reference sector to calculate differential slant column density (dSCD) over the whole domain of the GetoTASO measurements. CMAQ calculation over the reference sector (i.e., 6.75×10^{15} molecules cm^{-2}) was adopted as the reference SCD (SC_0), which is added to all dSCD values to convert to the SCD. The reference sector is known as a background area but is occasionally affected by the long-range transport of NO_2 from upwind areas. Considering the standard deviation of the OMI measurements accounts for such effects during the measurement period, we estimate the maximum uncertainties of the SC_0 can be calculated from this value (i.e., 1.33×10^{15} molecules cm^{-2}) in addition to the difference of the mean values between the CMAQ and OMI (i.e., 1.98×10^{15} molecules cm^{-2}). Therefore, our best estimate of the uncertainty of the SC_0 is the root of the sum of squares of these values (i.e., 2.38×10^{15} molecules cm^{-2}).

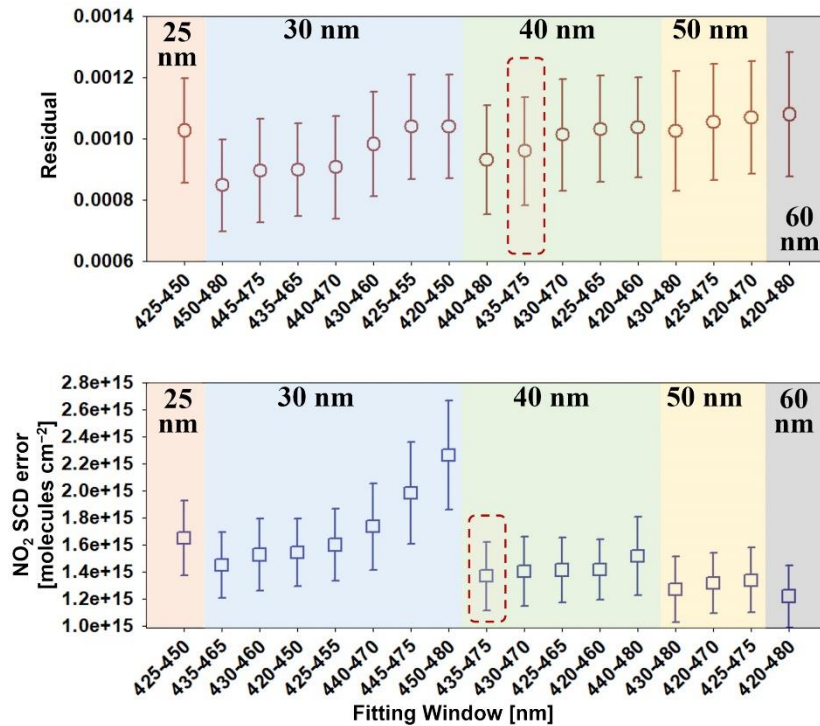
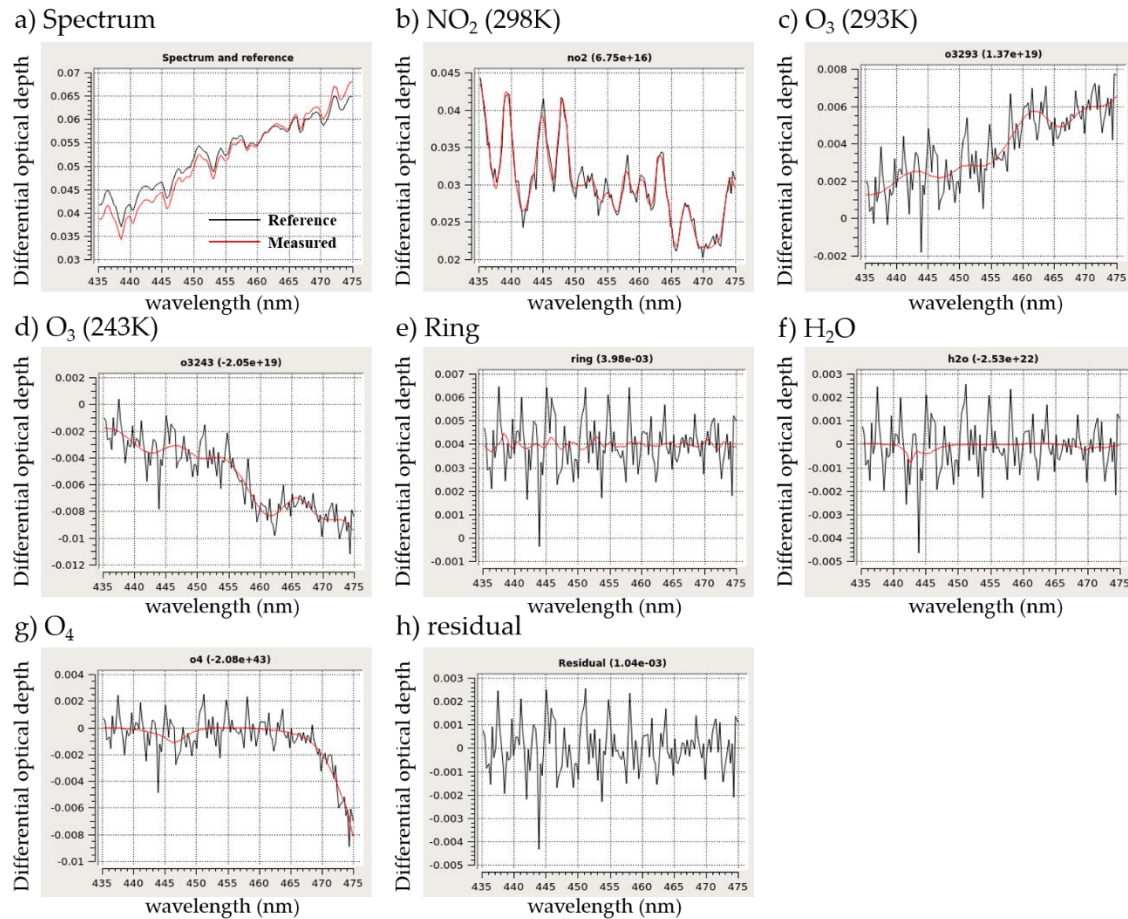


Figure 3. Residuals and NO_2 SCD errors of 17 spectral fitting window candidates (May 17, 2016, across track number: 15).

The spectral fitting window was selected based on the sensitivity test with 17 fitting window candidates from 420 to 480 nm with the length of the fitting window from 25 to 60 nm. Spectral fitting residuals and NO_2 SCD errors have been investigated for 17 spectral fitting window candidates (Fig. 3).

211 In terms of the residual, when the NO₂ fitting window includes a wavelength region less than 430 nm, it has a larger residual
 212 compared to the case where it does not. The higher residual can include the more noise signals that cannot be calculated
 213 mathematically, which can become an uncertainty for the NO₂ SCD retrievals. Therefore, we excluded the fitting window
 214 which includes wavelengths less than 430 nm for the GeoTASO NO₂ retrievals during the KORUS-AQ campaign. In the case
 215 of the NO₂ SCD error, it was confirmed that the longer the fitting window length, the lower the NO₂ SCD error appeared
 216 regardless of including the wavelength region less than 430 nm. Therefore, for the stable NO₂ SCD retrieval, an appropriate
 217 spectral fitting window needs to be selected which can minimize the residual with a moderate length of the fitting window. To
 218 find the optimal fitting window, we set the threshold value based on the above results: residual < 0.001, NO₂ SCD error < 1.4
 219 $\times 10^{15}$ molecules cm⁻², the length of fitting window > 30 nm. Then, the fitting window of 435–475 nm was selected for the
 220 GeoTASO NO₂ retrievals during the KORUS-AQ campaign. To determine the wavelength registration more accurately in the
 221 narrow fitting window, additional wavelength calibration of the spectra for each of the 33 across track pixels was performed
 222 using a high-resolution solar reference spectrum (Kurucz solar spectrum) (Chance and Kurucz, 2010) with the GDF. The
 223 absorption cross-sections of NO₂ (Vandaele et al., 1998), O₃ (Bogumil et al., 2000), H₂O (Rothman et al., 2010), and the Ring
 224 effect as pseudo-absorbers (Chance and Spurr, 1997) were used to construct the model equation; and B(λ), R(λ), A(λ), and
 225 N(λ) are the broad absorption of trace gases, extinction by Mie and Rayleigh scattering, variation in the spectral sensitivity of
 226 the detector or spectrograph, and noise, respectively, which were accounted for by an 8th order polynomial. An example of the
 227 spectral fitting results is presented in Fig. 4.
 228



229
 230 **Figure 4.** An example of the spectral fitting results of NO₂ retrievals from GeoTASO during the KORUS-AQ campaign (at Gangnam,
 231 Seoul on June 9, 2016). Red and black line in the panel (a) represent measured and reference spectrum, respectively. The panels of
 232 (b) to (h) depict examples of spectral fitting results of (b) NO₂, (c) O₃ (293 K), (d) O₃ (243 K), (e) ring, (f) H₂O, (g) O₄, where red and
 233 black lines are the absorption cross section of target species and the fitting residual plus the absorption of the target species,
 234 respectively. The panel (h) indicates the fitting residual of this example.

236 2.4.2 NO₂ AMF calculation

237 AMF, the ratio of SCD to VCD, can be calculated using the scattering weight (ω) and shape factor (S) (Palmer et al., 2001) in
 238 Eq. (2)–(5).

$$239 \quad AMF = \frac{SCD}{VCD'} \quad (2)$$

$$240 \quad AMF = AMF_G \int_{z_1}^{z_2} \omega(z) S(z) dz, \quad (3)$$

$$241 \quad \omega(z) = - \frac{1}{AMF_G} \frac{\partial \ln I_B}{\partial \tau}, \quad (4)$$

$$242 \quad S(z) = \frac{\alpha(z)n(z)}{\int_{z_1}^{z_2} \alpha(z)n(z) dz'} \quad (5)$$

243

244 Where AMF_G represents the geometric AMF, I_B is the earthshine radiance, τ is the optical depth, α is the absorption cross-
 245 section, and n is the number density of the absorber. NO₂ AMF was calculated using a linearized pseudo-spherical scalar and
 246 vector discrete ordinate radiative transfer model (VLIDORT, version 2.6; Spurr and Christi, 2014). Aerosol properties, such
 247 as AOD, SSA, APH, and *a priori* NO₂ vertical profile information, were simulated using the CMAQ, and surface reflectivity
 248 was obtained from MODIS (Collection 6). The SR products, MCD43A3, available at a 500 m spatial resolution, provide an
 249 estimate of the surface spectral reflectance including MODIS bands 1 through 7. Here, MODIS band 3 (459–479 nm) was
 250 used, because this band is the closest the wavelength (455 nm) used in the calculation of AMF in this study. APH was assumed
 251 to be the peak height of the aerosol extinction coefficient simulated in CMAQ, and the aerosol profile applied GDF based on
 252 APH (Hong et al., 2017). For pixels without reflectance information, AMF was not calculated. The products were corrected
 253 for atmospheric conditions, such as aerosol, gases, and Rayleigh scattering. In previous studies (Lamsal et al., 2017; Nowlan
 254 et al., 2018; Judd et al., 2019; Chong et al., 2020), an AMF was described for both above and below aircraft altitude is used to
 255 convert NO₂ SCDs to VCDs using Eq. (6)–(8).

$$256 \quad AMF \uparrow = AMF_G \int_{z_A}^{z_{TOA}} \omega(z) S(z) dz, \quad (6)$$

$$257 \quad AMF \downarrow = AMF_G \int_{z_0}^{z_A} \omega(z) S(z) dz, \quad (7)$$

$$258 \quad NO_2 \text{ VCD} \downarrow = \frac{NO_2 \text{ SCD} - AMF \uparrow \cdot NO_2 \text{ VCD} \uparrow}{AMF \downarrow}, \quad (8)$$

259 Where $AMF \uparrow$ and $AMF \downarrow$ are AMF above and below aircraft, respectively, and $NO_2 \text{ VCD} \uparrow$ represents NO₂ VCD above the
 260 aircraft obtained from a chemical transport model (CTM). However, here we calculated $NO_2 \text{ VCD} \downarrow$ by dividing NO₂ SCDs
 261 by $AMF \downarrow$ as the CMAQ only simulates the troposphere (surface to 50 hPa). However, as the stratospheric and free tropospheric
 262 NO₂ ($NO_2 \text{ VCD} \uparrow$) column densities over megacities and industrial areas are much lower than tropospheric NO₂ column
 263 densities, (Valks et al., 2011), we assume that the uncertainties in the AMF without considering the upper atmosphere are
 264 negligible in this study.

265

266 2.5 Chemical model description

267 Vertical profiles from CMAQ (Byun and Ching, 1999; Byun and Schere, 2006), a CTM, were used to calculate AMFs. The
 268 CMAQ simulations were conducted with a horizontal resolution of 15×15 km and had 27 vertical layers from the surface to
 269 50 hPa. The meteorological fields were prepared using the advanced research Weather Research and Forecasting (WRF)
 270 Advanced Research WRF (ARW) Model (Skamarock et al., 2008). Anthropogenic emissions were generated based on the
 271 KORUS v5.0 model (Woo et al., 2012), and biogenic emissions were simulated using the Model of Emissions of Gases and
 272 Aerosols from Nature (MEGAN v2.1; Guenther et al., 2006; 2012). Besides anthropogenic and biogenic emissions, the Fire
 273 Inventory from NCAR (FINN; Wiedinmyer et al., 2006, 2011) was used to update the pyrogenic emission fields.

274 The CMAQ AOD was calculated by integrating the aerosol extinction coefficient (Q_{ext}), which is the sum of scattering (Q_{sca})
 275 and absorption (Q_{abs}) coefficients, over all vertical layers (z) as follows:

$$276 \quad AOD = \int Q_{ext}(z) dz = \int \{Q_{sca}(z) + Q_{abs}(z)\} dz, \quad (9)$$

$$277 \quad Q_{abs}[Mm^{-1}] = \sum_i \sum_j \{ (1 - \omega_{ij}) \cdot \beta_{ij} \cdot f_{ij}(RH) \cdot [C]_{ij} \}, \quad (10)$$

$$278 \quad Q_{sca}[Mm^{-1}] = \sum_i \sum_j \{ \omega_{ij} \cdot \beta_{ij} \cdot f_{ij}(RH) \cdot [C]_{ij} \}, \quad (11)$$

279 Here, ω_{ij} indicates SSA of particulate species i for the particulate mode (or size bin) j , β_{ij} denotes the mass extinction
 280 efficiency, $f_{ij}(RH)$ is the hygroscopicity factor according to the relative humidity (RH), and $[C]_{ij}$ is the concentration of
 281 particulate species. CMAQ SSA is defined as the ratio of the integrated Q_{sca} to AOD, and NO_2 vertical profiles were obtained
 282 from NO_2 concentrations at each vertical layers by conducting CMAQ simulations. Details of the model descriptions and
 283 calculations of optical properties are given by Lee et al. (2020) and Malm and Hand (2007).

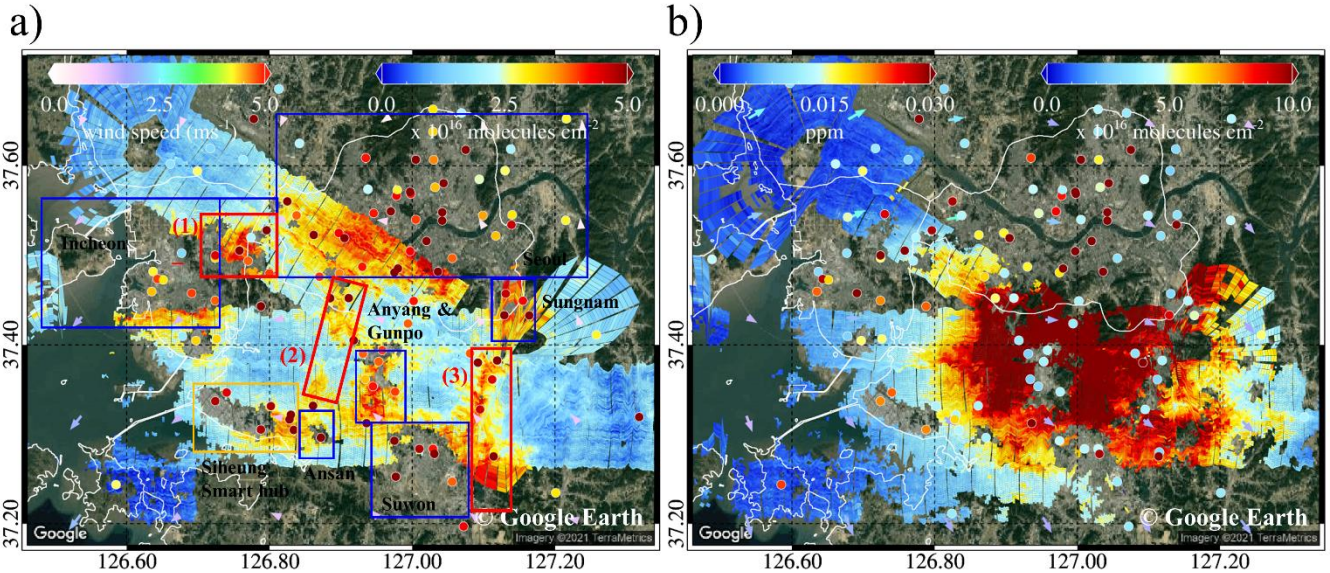
284 3 Results and discussion

285 3.1 NO_2 VCD retrieval

286 3.1.1 Seoul metropolitan region

287 We show the final NO_2 VCDs from 250 m spatial resolution. Because of NO_2 VCD, we selected the dates observed in both
 288 the morning and afternoon during the KORUS-AQ period over the Seoul metropolitan area, Busan, and Anmyeon. The
 289 retrieved dates for NO_2 VCDs were Jun 5, 9, and 10, 2016.

290 The population of the Seoul metropolitan region is approximately 20 million, which is approximately 40% of the total
 291 population of South Korea. It is rare to obtain high-resolution horizontal NO_2 VCD distributions using airborne measurements
 292 in the morning and afternoon, especially in Asian megacities. Figure 5 indicates tropospheric NO_2 VCDs over Seoul on June
 293 9 2016, at 9 AM and 3 PM local time (LT). Because of an issue with imaging systems, enlarged views (Fig. 5-Fig. 8) present
 294 a slightly stripy appearance from the GeoTASO observation (Nowlan et al., 2016; Chong et al., 2020).



295 **Figure 5. Tropospheric NO_2 VCD, in the Seoul metropolitan region on June 9, 2016, retrieved from GeoTASO: a) at 9 AM and b)**
 296 **at 3 PM. The red boxes represent expressways (counterclockwise from left to right, (1) Gyeongin Expressway, (2) Seohaean**
 297 **Expressway, and (3) Gyeongbu Expressway), the orange box indicates the industrial complex, and the blue boxes indicate the major**
 298 **cities (Seoul, Incheon, Suwon, Bucheon, Anyang, Gunpo, Sungnam, and Ansan) of the Seoul metropolitan region. Colors of the**
 299 **circles depict the NO_2 surface mixing ratio obtained from Air-Korea. The color arrows indicate the wind direction and speed at 1000**
 300 **hPa over Seoul metropolitan region, obtained via the Unified Model (UM) simulations (background RGB image is from Google**
 301 **Earth; <https://www.google.com/maps/>).**
 302

303

304 In the morning, NO₂ VCDs retrieved from GeoTASO were highly correlated with expressways (red boxes in Fig. 5), such as
305 the Gyeongin, Seohaean, and Gyeongbu Expressways, and over major cities with heavy traffic, such as Seoul, Bucheon, Ansan,
306 Anyang, and Suwon. GeoTASO observed NO₂ VCD values three-times higher ($>3 \times 10^{16}$ molecules cm⁻²) in these areas
307 compared to the surrounding rural areas. High NO₂ VCD values above 6×10^{16} molecules cm⁻² were observed above the
308 Gyeongin Expressway, which has very heavy traffic in a relatively short section, and the Gunpo Complex Logistics zone,
309 where diesel vehicle traffic is also high. The main NO₂ source regions and the regions where high NO₂ VCD values were
310 observed were highly consistent at 9 AM because the wind speed at this time—as obtained from the unified model (UM) based
311 Regional Data Assimilation and Prediction System (RDAPS) of the Korea Meteorological Administration (KMA)—was as
312 low as 0.1 ms⁻¹ and the average wind direction was 84.7° at 1000 hPa over Seoul metropolitan region. The average daily traffic
313 volume of these expressways exceeds 150,000 vehicles, and the total number of vehicles registered in these major cities is >
314 6,000,000, with an average daily mileage per car per day of over 38 km. Detailed information on these cities and expressways
315 is listed in Table 3 and 4. Based on the level of vehicular traffic, combustion using gasoline and diesel engines leads to high
316 overall emissions of NO₂ in the Seoul metropolitan region (Kendrick et al., 2015).

317

318 **Table 3. The population, number of registered vehicles, and average mileage per car per day of the major cities in the Seoul**
319 **and Busan metropolitan region obtained from the Korean Statistical Information Service (<https://kosis.kr/eng>).**

City	Population (millions)	Vehicle registration number (thousands)	Average mileage (km car ⁻¹ day ⁻¹)
Seoul	9.776	3,083	37.1
Incheon	2.914	1,402	41.7
Bucheon	0.848	284	37.2
Ansan	0.744	289	40.8
Anyang	0.596	206	39.6
Gunpo	0.286	87	38.8
Suwon	1.241	467	38.1
Sungnam	0.994	358	36.3
Busan	3.389	1,295	40.1
Daegu	2.450	1,121	37.1
Changwon	1.080	551	37.5
Kimhae	0.529	250	38.0

320

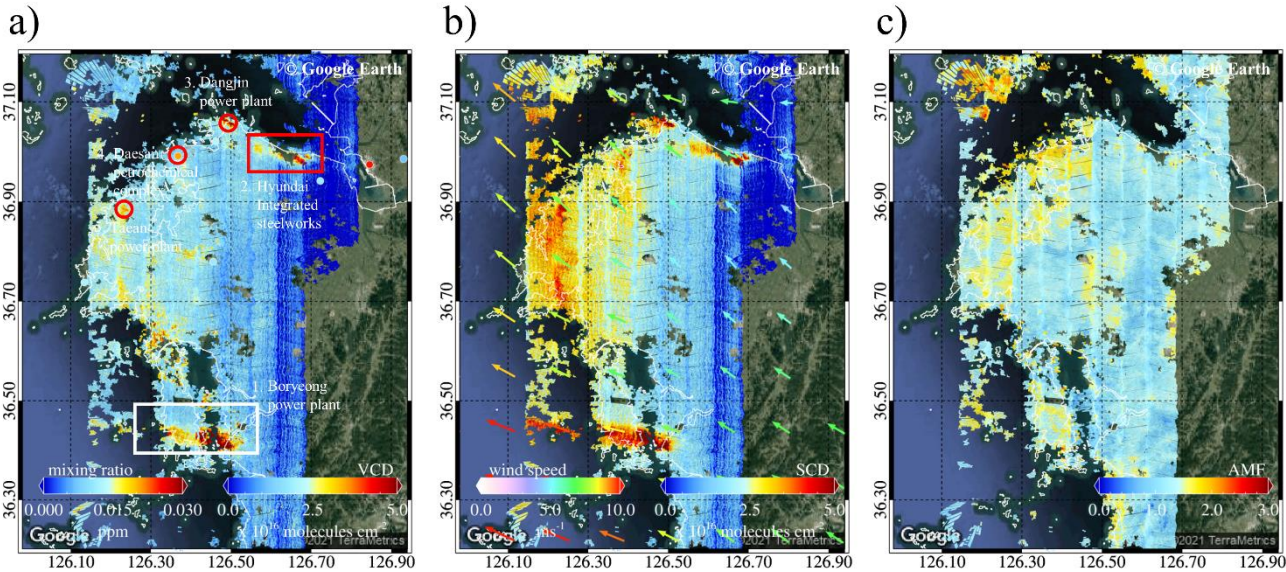
321 **Table 4. Daily average traffic volume on the Gyeongin, Gyeongbu, and Seohaean Expressways obtained using the Traffic**
322 **Monitoring System (<https://www.road.re.kr>).**

Expressway	Daily average traffic volume
Gyeongin Expressway	162,369
Gyeongbu Expressway	173,413
Seohaean Expressway	150,298

323

324 Compared to the data of the morning, the average wind speed and wind direction were 1.7 ms^{-1} and 284.5° at 1000 hPa in the
 325 afternoon and the afternoon had extremely high tropospheric NO_2 VCD values (exceeding $5 \times 10^{16} \text{ molecules cm}^{-2}$) in most of
 326 the Seoul metropolitan regions including rural areas, whereas the NO_2 mixing ratio (MR) obtained from Air-Korea decreases
 327 in the afternoon. According to Tzortziou et al. (2018), similar results were retrieved from the Pandora site in Seoul, with higher
 328 afternoon NO_2 VCDs than in the morning. This result is because the amount of NO_2 produced by chemical conversion of nitric
 329 oxide (NO) by O_3 and VOCs in the atmosphere, along with NO_x generated by regional emissions (traffic) in the Seoul
 330 metropolitan region, is greater than the amount lost by photolysis and transport to nearby areas (Herman et al., 2018).
 331 Furthermore, the increase in tropospheric NO_2 VCD in the afternoon is likely due to the accumulation and dispersion of NO_2
 332 according to the height of the change in the planetary boundary layer (Ma et al., 2013).

333 3.1.2 Industrial and power plant regions in Anmyeon



334
 335 **Figure 6. a) Tropospheric NO_2 VCD and b) NO_2 SCD retrieved from GeoTASO, and c) NO_2 AMF, native resolution (250 m)**
 336 **calculated using VLIDORT over Anmyeon in South Korea on June 5, 2016. The colored arrows indicate wind speed and wind**
 337 **direction at 850 hPa from the Unified Model (UM) simulations. The red circles and rectangle in panel (a) represent the major NO_2**
 338 **emission sources, such as steelworks and power plants (background RGB image is from Google Earth;**
 339 **<https://www.google.com/maps/>).**

340
 341 The high spatial resolution of the tropospheric NO_2 VCD from GeoTASO over the Anmyeon industrial region, where many
 342 industrial facilities and several power plants are distributed, is shown in Fig. 6. Panels a and b of this figure indicate
 343 tropospheric NO_2 VCD and NO_2 SCD retrieved from GeoTASO L1B data, respectively, between 13:00 and 17:00 LT on June
 344 5, 2016. Panel c depicts the calculated AMF of NO_2 from native resolution over the domain. GeoTASO observations detected
 345 moderate and strong NO_2 emission sources in this area: (1) Boryeong power plant, (2) Hyundai integrated steelworks, (3)
 346 Dangjin power plant, (4) Daesan Petrochemical Complex, and (5) Taean Power Plant. High NO_2 VCD values ($> 5 \times 10^{16}$
 347 molecules cm^{-2}) were observed over steel mill works, petrochemical complexes, and power plants, whereas values were
 348 comparatively low ($< 1 \times 10^{16}$ molecules cm^{-2}) over small cities including Seosan, Dangjin, and Boryeong with populations of
 349 less than 0.1 million, and the Seohaean Expressway. In 2016, the annual NO_x emissions from Hyundai steelworks and the
 350 Dangjin and Boryeong power plants were approximately 10.3, 11.9, and 16.8 kt year $^{-1}$, respectively. The NO_x emission rates
 351 of major industrial facilities in the Anmyeon region are shown in Table 5.

352

353 Table 5. NOx emission rates in 2016 from major industrial facilities in the Anmyeon region obtained from the Continuous
354 Emission Monitoring System of the Korea Environment Corporation (<https://www.stacknsky.or.kr/eng/index.html>).

Industrial facilities	NOx emission rate (kg year ⁻¹)
Boryeong power plant	16,788,438
Hyundai integrated steelworks	10,271,075
Dangjin power plant	11,852,972
Daesan petrochemical complex	3,397,939
Taeon power plant	15,466,022

355

Figure 6 shows high NO₂ concentrations of the main industrial facilities in the Anmyeon region, where the combustion of fossil fuel in factories and thermal power plants leads to high emissions (Prasad et al., 2012). Due to relatively sparse distribution over rural areas, the Air-Korea measurements did not detect the major NO₂ plume as shown in Fig. 6a. Thus, airborne remote sensing systems, such as GeoTASO, can effectively complement ground-based networks for monitoring minor and major NO_x emissions, particularly over these remote industrial regions.

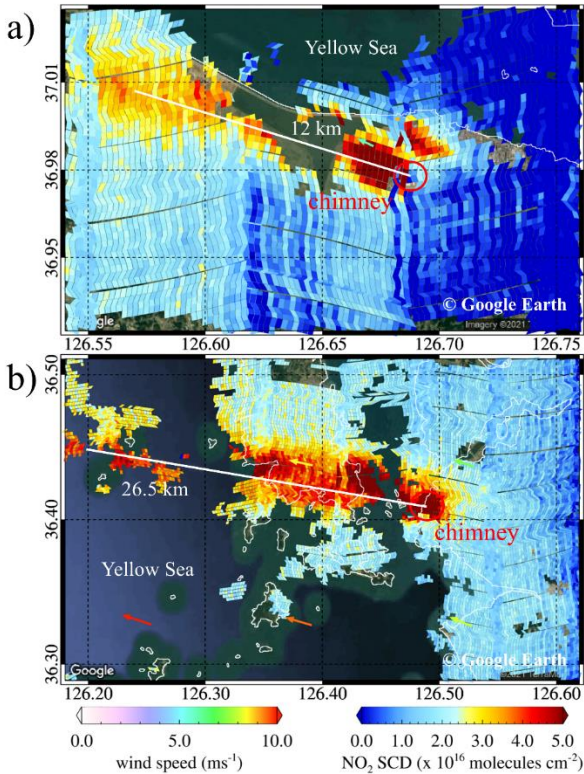
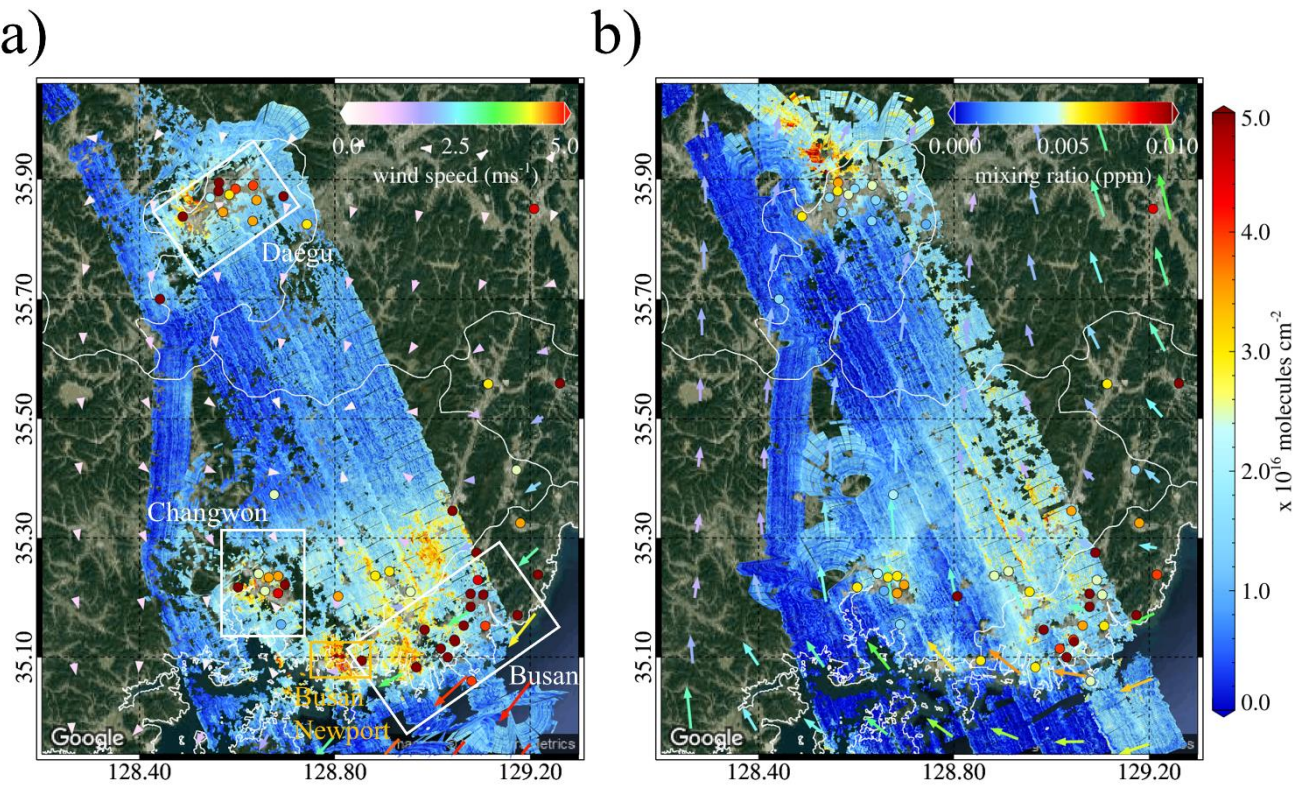


Figure 7. Enlarged view of GeoTASO tropospheric NO₂ SCD observation over a) Hyundai steel works, indicated by the red box in Figure 6, and b) the Boryeong power plant, indicated by the white box in Figure 6. The arrows represent the wind direction and speed at 850 hPa from the Unified Model (UM) simulations, respectively (background RGB image is from Google Earth; <https://www.google.com/maps/>).

The GeoTASO data captured not only NO_x emissions from the chimneys of steelworks and power plants but also its transport by the wind. Figure 7a and 7b show enlarged views of tropospheric NO₂ SCD retrieved using GeoTASO over the Hyundai steelworks (red box in Fig. 6) and the Boryeong power plant (white box in Fig. 6). The arrows in Fig. 7 represent the prevailing wind direction and speed from RDAPS. NO₂ emitted from the chimneys of these sites was transported to the Yellow Sea, traveling distances of over 26.5 km at speeds of approximately 6 ms⁻¹. According to Chong et al. (2020), similar results were found for SO₂ emitted and transported from these sites.



374
375 **Figure 8. Tropospheric NO₂ VCD in the Busan metropolitan region in the (a) morning and (b) afternoon of June 10, 2016.**
376 **The wind speed (colors scale) and wind direction (arrows) at 1000 hPa pressure level were obtained from the Unified Model (UM)**
377 **simulations. The white boxes represent major cities such as Busan, Daegu, and Changwon. The orange box represents Busan**
378 **Newport (the background RGB image is from Google Earth; <https://www.google.com/maps/>).**

379
380 Figure 8a and 8b show tropospheric NO₂ VCD retrieved from the GeoTASO L1B data over the Busan metropolitan region on
381 June 10 2016 in the morning (between 08:00 and 11:00 LT) and afternoon (between 13:00 and 16:00 LT), respectively. The
382 arrows in Fig. 8 indicate the wind speed and wind direction of 1000 hPa obtained from the UM-RDAPS, with the average
383 wind speed and wind direction of 0.9 ms⁻¹, and 55.4°, 1.9 ms⁻¹ and 147.0°, respectively, in the morning and afternoon. High
384 NO₂ VCDs were observed above urban areas, port, industrial complexes, and the inter-city road between Busan and Changwon.
385 Like the Seoul metropolitan regions, combustion using gasoline and diesel engines is estimated to contribute to the high NO_x
386 emission. In the morning, NO₂ VCDs were high (approximately 3 × 10¹⁶ molecules cm⁻²) in the major cities and, especially,
387 around Busan Newport, with values exceeding 7 × 10¹⁶ molecules cm⁻². In comparison, in the mountainous regions between
388 Daegu and Busan, the NO₂ VCD values were less than 1 × 10¹⁶ molecules cm⁻² during the same period. The spatial distribution
389 of tropospheric NO₂ VCDs was like that in the Seoul metropolitan regions, with high values over major cities and roads
390 (compare Figs. 5 and 8). In Busan, fossil fuel combustion that uses both road vehicles and ships is likely to contribute to the
391 NO_x emissions. In the afternoon, unlike the Seoul metropolitan region, tropospheric NO₂ VCD over Busan decreased by over
392 3 × 10¹⁶ molecules cm⁻², which also corresponds with NO₂ MR data obtained from the Air-Korea sites. Detailed information
393 on these cities is listed in Table 3.

394

3.2 Error estimation

The accuracy of the NO₂ VCD retrieval using the DOAS method depends on both the AMF calculation and the spectral fitting error of the SCD retrieval. Retrieval errors of the NO₂ VCD were estimated using error propagation analysis as expressed in Eq. (12).

$$\frac{\varepsilon_{VCD}}{VCD} = \sqrt{\left(\frac{\varepsilon_{SCD}}{SCD}\right)^2 + \left(\frac{\varepsilon_{AMF}}{AMF}\right)^2}, \quad (12)$$

Where ε_{VCD} is the total error of NO₂ VCD. The error of NO₂ SCD (ε_{SCD}) is obtained from the spectral fitting error of NO₂ SCD via the DOAS spectral fitting. ε_{AMF} indicates the error of NO₂ AMF caused by uncertainties in the model input parameters for AMF calculation. Uncertainties in aerosol properties (AOD, SSA, and APH) and SR for the RTM calculations are the major factors affecting NO₂ AMF accuracy (Boersma et al., 2004; Leitão et al., 2010; Hong et al., 2017). Therefore, in this present study, we quantified the NO₂ AMF errors (ε_{AMF}) due to uncertainties in the input parameters independent of each other using Eq. (13):

$$\varepsilon_{AMF} = \sqrt{\left(\frac{\partial AMF}{\partial AOD}\right)^2 \sigma AOD^2 + \left(\frac{\partial AMF}{\partial SSA}\right)^2 \sigma SSA^2 + \left(\frac{\partial AMF}{\partial ALH}\right)^2 \sigma ALH^2 + \left(\frac{\partial AMF}{\partial SR}\right)^2 \sigma SR^2} = \sqrt{\sum_{i=1}^4 \left(\frac{\partial AMF}{\partial \chi_i}\right)^2 \sigma_{\chi_i}^2}, \quad (13)$$

where $\frac{\partial AMF}{\partial \chi_i}$ are partial derivatives of NO₂ AMF regarding the input parameters (χ_i), σ_{χ_i} represents the uncertainty of the χ_i . The σ of AOD, SSA, SR, and APH are assumed to be 30% (Ahn et al., 2014), 0.04 (Jethva et al., 2014), $0.005 + 0.05 \times SR$ (EOS Land Validation; <https://landval.gsfc.nasa.gov>), and 1 km (Fishman et al., 2012), respectively, in this study. To derive $\left(\frac{\partial AMF}{\partial \chi_i}\right)^2$, the true χ_i is input to the RTM to simulate ‘true’ NO₂ AMF. For the AOD, SSA, APH, and SR, perturbed NO₂ AMF was simulated using RTM with $\chi_i \pm \sigma_{\chi_i}$. $\partial \chi_i$ denotes the difference between the ‘centre’ χ_i and $\chi_i \pm \sigma_{\chi_i}$, and ∂AMF is the difference between the ‘centre’ NO₂ AMF (AMF_{centre}) simulated with ‘centre’ input values and the perturbed NO₂ AMF ($AMF_{perturbed}$) simulated using the perturbed input parameters $\chi_i \pm \sigma_{\chi_i}$ (i.e. the original input parameters modified by the uncertainty). The simulation for calculating the ε_{AMF} was conducted using the input parameters on June 9, 2016.

Table 6. Total NO₂ VCD caused by uncertainties in NO₂ SCD and NO₂ AMF (the average for the flight on June 9, 2016).

NO ₂ AMF errors	AOD	2.8%
	SSA	4.1%
	Aerosol peak height	22.3%
	Surface reflectance	2.8%
	Total NO₂ AMF error due to aerosol uncertainties	23.3%
NO ₂ SCD error		11.7%
NO₂ VCD error		26.9%

Table 6 lists the estimated NO₂ VCD error on June 9, 2016 for each source based on the error propagation method. The error estimation was conducted for the pixels where root mean square residual < 0.001 and NO₂ VCD > 5×10^{15} molecules cm⁻² since NO₂ SCD precision is reported to be highly decreased in low NO₂ conditions (Hong et al., 2017). The total NO₂ VCD error was 26.9% with a high portion of NO₂ AMF error. The NO₂ SCD error was calculated to be 11.7%, showing the importance of accurate DOAS spectral fitting for deriving NO₂ SCD. The total AMF error due to uncertainties in the input

parameters was calculated to be 23.3%. Among model input parameters, the effect of APH on NO₂ AMF becomes high (22.3%), indicating the importance of accurate aerosol profile information. APH sensitively affects NO₂ AMF because near the surface where trace gases and aerosols are well mixed, aerosols lead to multiple scattering effects and the light absorption of trace gases is due to increasing light path (Castellanos et al., 2015; Hong et al., 2017). Especially, APH can be the most important input parameter in the Asia region where high loadings of aerosol plumes persist throughout the year. The NO₂ AMF calculation errors due to uncertainties in SSA and AOD were 4.1% and 2.8%, respectively. The NO₂ AMF calculation error due to uncertainties in aerosol optical properties (SSA and AOD) appears to be smaller than those in a previous study (Leitão et al., 2010). The smaller effect of the aerosol properties can be explained by the moderate aerosol loading (AOD = 0.40) on the day of flight day. The NO₂ AMF errors become larger under high AOD conditions. The smallest effect of SR was found on NO₂ AMF calculation error, which was calculated based on the uncertainty of the SR of the satellite-based product (MODIS). Therefore, it may be an unrealistic number for the airborne NO₂ AMF calculation. Once the uncertainty of airborne-based SR is provided, considering its measurement geometry and finer spatial resolution, more realistic airborne-based NO₂ AMF calculation error due to uncertainties in SR can be estimated. The can of the *a priori* NO₂ profile shape also be a factor to cause calculation error for NO₂ AMF, as reported in previous studies (Leitão et al., 2010, Meier et al., 2016, Hong et al., 2017). Therefore, it is necessary to calculate the contribution of the shape of the *a priori* NO₂ profile on the accuracy of NO₂ AMF in the future. Moreover, the resulting uncertainties of input parameters of a GeoTASO ground pixel need to be considered by combining the initial uncertainties of CTM and satellite-based products, and by the variability of the parameters within the respective CTM (AOD, SSA, and APH) and satellite (SR) grid box. If values such as SR are assumed constant over larger areas, the fundamental spatial variability in this these data increases the uncertainty of the AMF and hence of the determined NO₂ VCD on the respective finer spatial scale. In addition, the uncertainty from the assumption on the SC₀ and the uncertainty from ignoring the NO₂ above the aircraft in the AMF calculations are needed to be considered in the error analysis. This analysis should be considered in further study.

$$AMF_{percent_change} = \frac{AMF_{perturbed} - AMF_{centre}}{AMF_{centre}} \times 100, \quad (14)$$

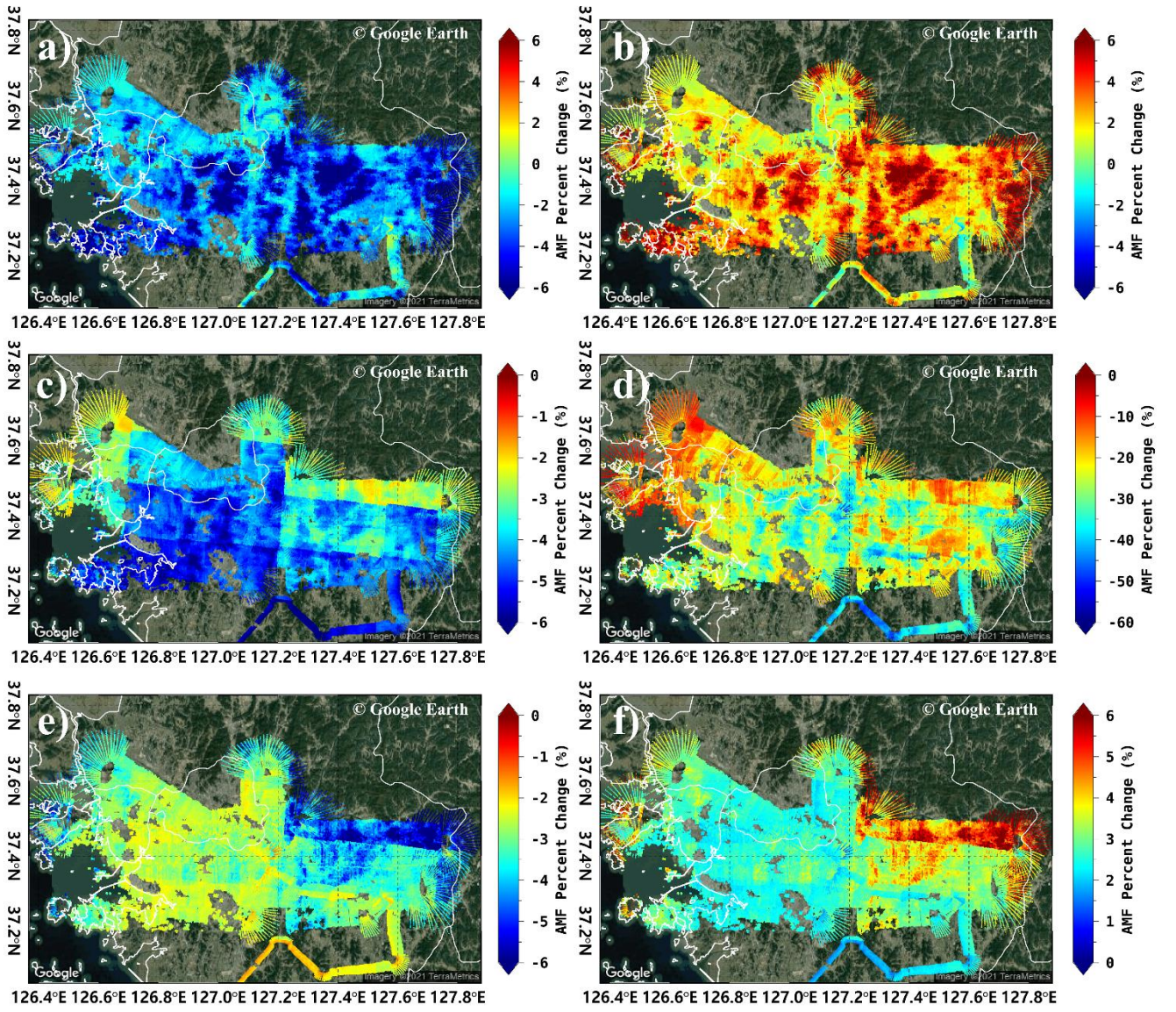


Figure 9. Percent change between AMF calculated using the CMAQ model simulation and those using a) 30% lower AOD, b) 30% higher AOD, c) 0.04 lower SSA, d) 1km higher APH, compared to the model outputs. The percentage change for AMF calculated using MODIS data and those using e) $0.005 + 0.05 \times \text{SR}$ lower SR, f) $0.005 + 0.05 \times \text{SR}$ higher SR (background RGB image is from Google Earth; <https://www.google.com/maps/>).

In this study, we also investigated the spatial distribution of AMF calculation errors associated with uncertainties in aerosol properties (AOD, SSA, and APH) and SR. The percent change in NO_2 AMF ($\text{AMF}_{\text{percent_change}}$) was calculated on each spatial pixel using Eq. (14). Figure 9a and 9b indicate the percentage change error between the calculated AMFs using the CMAQ AOD data with 30% lower (Fig. 9a) and 30% higher (Fig. 9b) values, respectively. The AMF decreased and increased by up to 10% with decreasing and increasing AOD, respectively, in the Seoul metropolitan region. We estimated that, under low aerosol loading conditions, an increase in AOD near the surface leads to an increase in the scattering probability within the surface layer with high NO_2 concentrations. Figure 9c indicates the percent change error between the calculated AMFs using CMAQ SSA data with a 0.04 lower value. The AMF decreased with decreasing SSA because the absorption of light increased. APH was also found to highly affect the accuracy of the AMF calculations (Fig. 9d). The APH uncertainty of 1 km decreased the AMFs with an average $\text{AMF}_{\text{percent_change}}$ of -25% on the flight day. Especially, on the pixels where $\text{AOD} > 0.6$, the average $\text{AMF}_{\text{percent_change}}$ was found to be -26% whereas that was -27% on the pixels where $\text{AOD} < 0.4$, showing the combined effect of aerosol loading and aerosol profile shape on the NO_2 AMF calculations. Figure 9e and 9f indicate the percentage change

error between the calculated AMFs using the MODIS SR data with $0.005 + 0.05 \times \text{SR}$ lower (Fig. 9e) and $0.005 + 0.05 \times \text{SR}$ higher (Fig. 9f) values, respectively. The AMF decreased by approximately 3% when the SR decreases, and vice versa when it increased.

3.3 Validation of NO₂ VCDs retrieved from GeoTASO

The tropospheric NO₂ VCDs retrieved from GeoTASO L1B data (NO_{2,G}) were compared with those obtained from OMI total NO₂ VCDs (NO_{2,O}) and Pandora (NO_{2,P}). The NO_{2,O} were only available for June 10 during the campaign period. Therefore, we compared only 48 NO_{2,G} and NO_{2,O} data points within a radius of 20 km and 30 min, which yielded a correlation coefficient of 0.48 with a slope of 0.13 (Fig. 10 a). To validate, All NO_{2,G} within a radius 20 km of the OMI center coordinate were averaged.

The NO₂ values are relatively low, as GeoTASO observation is conducted in a region with low NO₂ compared to the Seoul metropolitan and the overpass time of OMI is approximately 13:30 LT when NO₂ decreased. The low slope value is because the OMI with low spatial resolution does not reflect the spatial NO₂ inhomogeneity in the pixel.

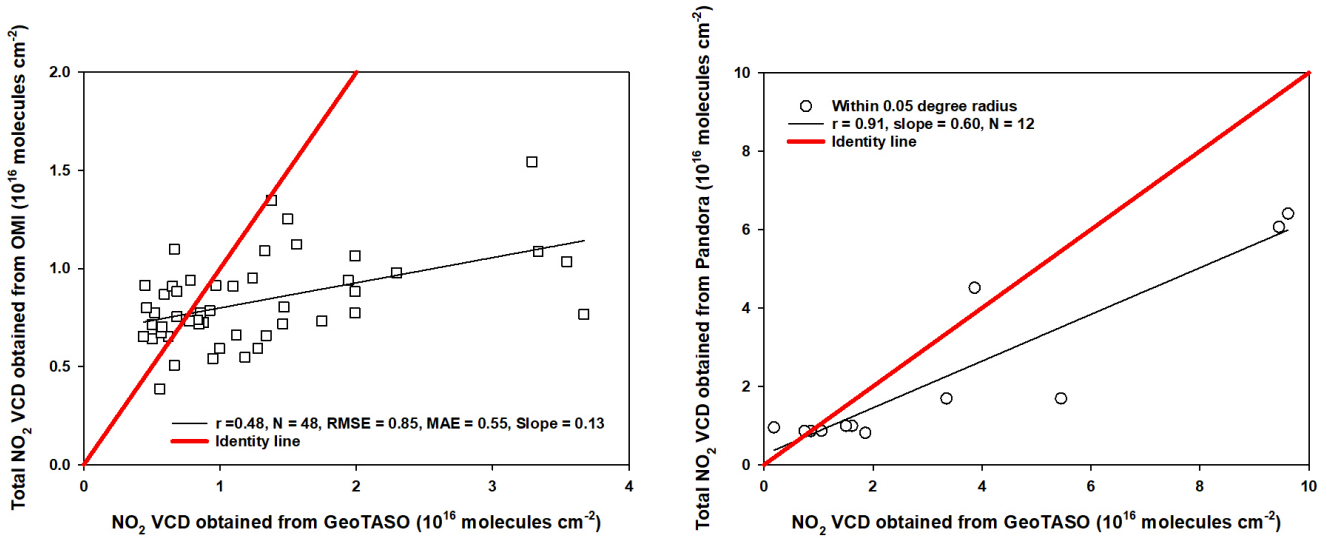
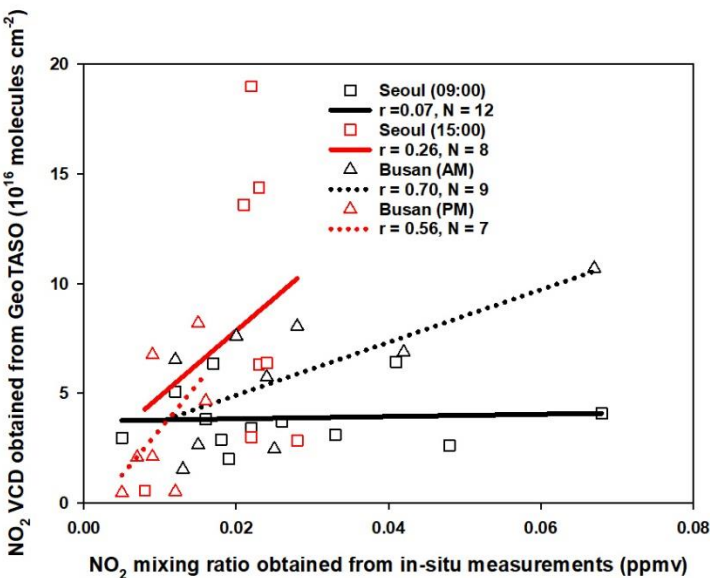


Figure 10. Scatter plots of a) NO₂ VCD retrieved from GeoTASO and total NO₂ VCD obtained from OMI and b) total NO₂ VCD obtained from Pandora and NO₂ VCD retrieved from GeoTASO, respectively.

To compare NO_{2,G} data, we made a comparison with total NO₂ VCD obtained from the Pandora system (NO_{2,P}) during the KORUS-AQ campaign period. NO_{2,P} obtained from Busan University, Olympic Park, Songchon, Yeosu, and Yonsei University Pandora sites on June 5, 9, and 10 were used for the GeoTASO validation (Fig. 1). NO_{2,G} and NO_{2,P} columns at these sites are compared in Fig. 11. To compare NO_{2,G} and NO_{2,P}, we used averaged NO_{2,G} retrieved from 16 across tracks with the smallest viewing zenith angle and averaged 30 min NO₂ obtained from pandora measurement within a radius of approximately 0.05°. NO_{2,G} and NO_{2,P} were correlated ($R = 0.91$, with a slope of 0.60), however, when NO_{2,P} was lower than 1×10^{16} molecules cm⁻², the correlation coefficient between NO_{2,G} and NO_{2,P} was < 0.1 . The weak correlation at low NO₂ levels most likely reflects differences in viewing geometries and the horizontal inhomogeneity of the measured NO₂ between Pandora and GeoTASO. Furthermore, Pandora and GeoTASO can be used for the NO₂ validation of geostationary satellites, such as GEMS. However, because the number of pandora is limited in this campaign, we difficulty validating NO₂ retrieved from GeoTASO under various conditions. Many ground-based remote sensing measurements are needed to validate GEMS under various conditions.



496

497 **Figure 11.** Scatter plot of the NO₂ VCDs retrieved from GeoTASO, and NO₂ surface mixing ratio obtained from Air-Korea.
498 The black and red squares represent the NO₂ data at 9 AM and 3 PM (local time) in the Seoul metropolitan region,
499 respectively. The black and red triangles represent those in the morning and afternoon, over Busan, respectively.

500

501 To compare the spatiotemporal distribution of NO₂ VCDs retrieved from GeoTASO, NO_{2,G} compared with surface spatial
502 patterns, NO_{2,G} was compared with NO_{2,A} for GeoTASO data within a radius of approximately 0.05 km and 30 min (Fig. 11).
503 To compare NO_{2,G} and NO_{2,A}, we used averaged NO_{2,G} retrieved from 16 across tracks and averaged 30 min within a radius of
504 0.05°. Because in situ measurements provide NO₂ VMR (NO_{2,A})(ppmv) once per hour, NO_{2,A} of the nearest time is used to
505 compare with NO_{2,G}. The correlation coefficient (R) between NO_{2,G} (molecules cm⁻²) and NO_{2,A} at 9 AM and 3 PM LT in the
506 Seoul metropolitan region was 0.07 and 0.26, respectively. When using only roadside station data from Air-Korea, the R-value
507 for the morning increased to 0.72, which implies GeoTASO is more sensitive to emissions from NO₂ source areas, such as
508 roadsides (Fig. 5). Because the comparison, there were large differences in the morning and afternoon. These results were
509 identified because synoptic meteorology played an important role from June 1 to June 10, 2016 (Choi et al., 2019). As described
510 by Judd et al. (2018), the spatial distribution for NO₂ VCDs appears to reflect the emission source in local industrialized regions
511 and transportations in the morning with relatively weak winds. NO₂ concentration often increases in the late morning,
512 indicating that the emission process proceeds faster than the NO₂ removal process. As the planetary boundary layer heights
513 (PBLH) in early afternoon increase and surface NO₂ is mixed through a deeper PBLH, the NO₂ VCDs distribution showed a
514 wider increase in most of the Seoul metropolitan area and the column amounts continue to increase (Judd et al., 2018).
515 When comparing NO₂ VCDs with surface NO₂ concentrations, it should be highlighted that it is a nonlinear relationship
516 between NO_{2,G} and NO_{2,A}. Although it may vary depending on weather conditions, high NO₂ VCDs from airborne observations
517 can sometimes be detected with low surface NO₂ concentrations. When exhaust gases emitted from industrial facilities occur
518 at a certain altitude (stacks/chimneys), NO_{2,G} show high NO₂ VCDs, but NO_{2,A} may be observed to have a low concentration.
519 Unfortunately, in the Anmyeon industrial region, NO_{2,G} and NO_{2,A} could not be compared due to spatial restrictions because
520 the distribution of ground observation stations is concentrated in metropolitan areas.
521 In the Busan metropolitan area, the R-value of the NO_{2,G} and NO_{2,A} data had a correlation coefficient greater than 0.56. This
522 reflects the more even horizontal distribution of NO₂ in the afternoon, when diffusion from the source areas had occurred.
523 However, for a more accurate comparison, NO₂ VCD data should be converted to NO₂ MR based on mixing layer height,
524 temperature, and pressure profile data (Kim et al., 2017; Qin et al., 2017; Jeong and Hong, 2021a). However, because the
525 number of pandora and satellite data is limited in this campaign, we had difficulties in validating NO₂ retrieved from GeoTASO

under various conditions. Because ground-based, airborne and space borne remote sensing measurements have their own advantages and disadvantages, it is recommended a comprehensive observation campaign involving all of ground-based, airborne and space-borne measurements should be conducted continuously for the upcoming new era of geostationary environmental satellites.

4 Conclusions

For the first time, we have retrieved NO₂ VCD data using airborne GeoTASO observations over the Seoul metropolitan region—one of the most populous cities worldwide, the Busan metropolitan region—the second-largest city in South Korea, and Anmyeon, with thermal power plants and industrial complexes. By retrieving NO₂ data using GeoTASO L1B radiance, it was possible to observe the spatial distribution of NO₂ in these metropolitan and industrial regions. In the morning, tropospheric NO₂ VCD in Seoul showed a strong horizontal gradient between rural and urban areas. In urban areas, tropospheric NO₂ VCD was high, with values exceeding 3×10^{16} molecules cm⁻²; in rural areas, values were typically below 1×10^{16} molecules cm⁻². Extremely high values over 10×10^{16} molecules cm⁻² were also observed in both rural and urban areas. In Anmyeon, GeoTASO observations showed that NO₂ is mainly emitted from the chimneys of industrial complexes and thermal power plants, and subsequently transported by wind approximately 26.5 km to the Yellow Sea on the west coast of the Korean Peninsula. In the Busan metropolitan region, in the morning, tropospheric NO₂ VCDs showed a pattern similar to the Seoul metropolitan region, with high values above the inter-city road. However, unlike Seoul, tropospheric NO₂ VCDs in Busan decreased in the afternoon due to local different weather conditions locally.

To compare the data retrieved from the GeoTASO system, we compared NO_{2,G} with NO_{2,O} obtained from the OMI, NO_{2,A} obtained from Air-Korea, and NO_{2,P} obtained from the Pandora observation system. When the distance between two observations was below 20 km or 0.05° within 30 min, the correlation coefficients were relatively high (R = 0.48, and 0.91, respectively). However, the correlation between NO_{2,G} and NO_{2,A} over the Seoul metropolitan region was extremely weak (R = 0.07) in the morning because of the more pronounced NO₂ horizontal gradient.

The GeoTASO system successfully observed NO₂ VCDs with high horizontal spatial resolution for both metropolitan and industrial regions. This demonstrates that airborne remote sensing measurements from GeoTASO, similar to GCAS, APEX and others, can be an effective tool for the validation of trace gases retrieved from environmental satellites, including the OMI, TROPOMI, and GOME-2; these systems can obtain high-resolution measurements over relatively wide areas. However, to validate geostationary environmental satellites with higher spatiotemporal resolutions, such as the GEMS, TEMPO, and sentinel-4, additional validation strategies are needed. Based on error estimation, it can be concluded that aerosol properties are relevant and should be determined and NO₂ vertical profile retrieval performed using, for example, LIDAR, MAX-DOAS, and sondes. This is important because the accuracy of aerosol properties, surface reflectance and the NO₂ vertical profiles affects the accuracy of AMF calculations (Leitão et al., 2010; Hong et al., 2017; Lorente et al., 2017; Boersma et al., 2018). Furthermore, as we observed in the Seoul metropolitan area, closer spaced observations using ground-based remote sensing systems and in situ measurements are needed as NO₂ displays large horizontal gradients, especially in the morning.

Author contributions

GH and **HH** designed and implemented the research. **KL** provided the CTM data. **GH** developed the code for model running and performed the RTM simulations. **HH** and **UJ** contributed to the analysis of ground-based data. **GH** and **WC** conducted the sensitivity test. **GH**, **KL**, **HH**, **UJ**, **WC**, and **JJS** revised and edited the paper. **HH**, **UJ**, and **WC** provided constructive comments. All authors contributed to this works.

564 **Competing interests**

565 The authors declare that they have no conflict of interest.

566 **Acknowledgements**

567 Pandora data were obtained from the KORUS-AQ home pages of NASA's Goddard Space Flight Center
568 (<https://avdc.gsfc.nasa.gov/pub/DSCOVR/Pandora/DATA/KORUS-AQ/>). Ground-based NO₂ MR data were obtained
569 from Air-Korea (http://www.airkorea.or.kr/web/detailViewDown?pMENU_NO=125/). The authors would like to
570 thank KORUS-AQ campaign team for providing the GeoTASO and Pandora data.

571 **Funding**

572 This work was funded by the National Institute of Environmental Research (NIER) of the Ministry of Environment [No. NIER-
573 2021-01-01-100].

574 **References**

- 575 Boersma, K. F., Eskes, H. J., and Brinksma, E. J.: Error analysis for tropospheric NO₂ retrieval from space: ERROR
576 ANALYSIS FOR TROPOSPHERIC NO₂, *J. Geophys. Res.*, 109, n/a-n/a, <https://doi.org/10.1029/2003JD003962>, 2004.
- 577 Boersma, K. F., Eskes, H. J., Richter, A., De Smedt, I., Lorente, A., Beirle, S., van Geffen, J. H. G. M., Zara, M., Peters, E.,
578 Van Roozendael, M., Wagner, T., Maasakkers, J. D., van der A, R. J., Nightingale, J., De Rudder, A., Irie, H., Pinardi, G.,
579 Lambert, J.-C., and Compernelle, S. C.: Improving algorithms and uncertainty estimates for satellite NO₂ retrievals: results
580 from the quality assurance for the essential climate variables (QA4ECV) project, *Atmos. Meas. Tech.*, 11, 6651–6678,
581 <https://doi.org/10.5194/amt-11-6651-2018>, 2018.
- 582 Brauer, M., Hoek, G., Van Vliet, P., Meliefste, K., Fischer, P. H., Wijga, A., Koopman, L. P., Neijens, H. J., Gerritsen, J.,
583 Kerkhof, M., Heinrich, J., Bellander, T., and Brunekreef, B.: Air Pollution from Traffic and the Development of Respiratory
584 Infections and Asthmatic and Allergic Symptoms in Children, *Am J Respir Crit Care Med*, 166, 1092–1098,
585 <https://doi.org/10.1164/rccm.200108-007OC>, 2002.
- 586 Burrows, J. P., Hölzle, E., Goede, A. P. H., Visser, H., and Fricke, W.: SCIAMACHY—scanning imaging absorption
587 spectrometer for atmospheric chartography, *Acta Astronautica*, 35, 445–451, [https://doi.org/10.1016/0094-5765\(94\)00278-T](https://doi.org/10.1016/0094-5765(94)00278-T),
588 1995.
- 589 Burrows, J. P., Weber, M., Buchwitz, M., Rozanov, V., Ladstätter-Weissenmayer, A., Richter, A., DeBeek, R., Hoogen, R.,
590 Bramstedt, K., Eichmann, K.-U., Eisinger, M., and Perner, D.: The Global Ozone Monitoring Experiment (GOME): Mission
591 Concept and First Scientific Results, 56, 151–175, [https://doi.org/10.1175/1520-0469\(1999\)056<0151:TGOMEG>2.0.CO;2](https://doi.org/10.1175/1520-0469(1999)056<0151:TGOMEG>2.0.CO;2),
592 1999.
- 593 BYUN, D.: Science algorithms of the EPA Models-3 Community Multiscale Air Quality (CMAQ) Modeling System, 1999.
- 594 Byun, D. and Schere, K. L.: Review of the Governing Equations, Computational Algorithms, and Other Components of the
595 Models-3 Community Multiscale Air Quality (CMAQ) Modeling System, *Appl. Mech. Rev.*, 59, 51,
596 <https://doi.org/10.1115/1.2128636>, 2006.
- 597 Callies, J., Corpaccioli, E., Eisinger, M., Hahne, A., and Lefebvre, A.: GOME-2-Metop's second-generation sensor for
598 operational ozone monitoring, *ESA Bull*, 1, 28–36, 2000.
- 599 Castellanos, P., Boersma, K. F., Torres, O., and de Haan, J. F.: OMI tropospheric NO₂ air mass factors over South America:
600 effects of biomass burning aerosols, *Atmos. Meas. Tech.*, 8, 3831–3849, <https://doi.org/10.5194/amt-8-3831-2015>, 2015.

601 Chance, K. and Kurucz, R. L.: An improved high-resolution solar reference spectrum for earth's atmosphere measurements in
 602 the ultraviolet, visible, and near infrared, *Journal of Quantitative Spectroscopy and Radiative Transfer*, 111, 1289–1295,
 603 <https://doi.org/10.1016/j.jqsrt.2010.01.036>, 2010.

604 Chance, K. V. and Spurr, R. J. D.: Ring effect studies: Rayleigh scattering, including molecular parameters for rotational
 605 Raman scattering, and the Fraunhofer spectrum, *Appl. Opt.*, 36, 5224, <https://doi.org/10.1364/AO.36.005224>, 1997.

606 Choi, S., Lamsal, L. N., Follette-Cook, M., Joiner, J., Krotkov, N. A., Swartz, W. H., Pickering, K. E., Loughner, C. P., Appel,
 607 W., Pfister, G., Saide, P. E., Cohen, R. C., Weinheimer, A. J., and Herman, J. R.: Assessment of NO₂ observations during
 608 DISCOVER-AQ and KORUS-AQ field campaigns, *Atmos. Meas. Tech.*, 13, 2523–2546, [https://doi.org/10.5194/amt-13-](https://doi.org/10.5194/amt-13-2523-2020)
 609 2523-2020, 2020.

610 Choi, W. J.: Introducing the geostationary environment monitoring spectrometer, *J. Appl. Rem. Sens.*, 12, 1,
 611 <https://doi.org/10.1117/1.JRS.12.044005>, 2018.

612 Choi, M., Lim, H., Kim, J., Lee, S., Eck, T. F., Holben, B. N., Garay, M. J., Hyer, E. J., Saide, P. E., and Liu, H.: Validation,
 613 comparison, and integration of GOCI, AHI, MODIS, MISR, and VIIRS aerosol optical depth over East Asia during the 2016
 614 KORUS-AQ campaign, *Atmospheric Measurement Techniques*, 12(8), 4619–4641, <https://doi.org/10.5194/amt-12-4619-2019>,
 615 2019.

616 Chong, H., Lee, S., Kim, J., Jeong, U., Li, C., Krotkov, N. A., Nowlan, C. R., Al-Saadi, J. A., Janz, S. J., Kowalewski, M. G.,
 617 Ahn, M.-H., Kang, M., Joiner, J., Haffner, D. P., Hu, L., Castellanos, P., Huey, L. G., Choi, M., Song, C. H., Han, K. M., and
 618 Koo, J.-H.: High-resolution mapping of SO₂ using airborne observations from the GeoTASO instrument during the KORUS-
 619 AQ field study: PCA-based vertical column retrievals, *Remote Sensing of Environment*, 241, 111725,
 620 <https://doi.org/10.1016/j.rse.2020.111725>, 2020.

621 Choo, G.-H., Seo, J., Yoon, J., Kim, D.-R., and Lee, D.-W.: Analysis of long-term (2005–2018) trends in tropospheric NO₂
 622 percentiles over Northeast Asia, *Atmospheric Pollution Research*, 11, 1429–1440, <https://doi.org/10.1016/j.apr.2020.05.012>,
 623 2020.

624 Danckaert, T., Fayt, C., Van Roozendaal, M., De Smedt, I., Letocart, V., Merlaud, A., and Pinardi, G.: QDOAS Software user
 625 manual, Belgian Institute for Space Aeronomy, 2016.

626 de Foy, B., Lu, Z., and Streets, D. G.: Satellite NO₂ retrievals suggest China has exceeded its NO_x reduction goals from the
 627 twelfth Five-Year Plan, *Sci Rep*, 6, 35912, <https://doi.org/10.1038/srep35912>, 2016.

628 General, S., Pöhler, D., Sihler, H., Bobrowski, N., Frieß, U., Zielcke, J., Horbanski, M., Shepson, P. B., Stirm, B. H., Simpson,
 629 W. R., Weber, K., Fischer, C., and Platt, U.: The Heidelberg Airborne Imaging DOAS Instrument (HAIDI) - a novel imaging
 630 DOAS device for 2-D and 3-D imaging of trace gases and aerosols, *Atmos. Meas. Tech.*, 7, 3459–3485,
 631 <https://doi.org/10.5194/amt-7-3459-2014>, 2014.

632 Guenther, A., Karl, T., Harley, P., Wiedinmyer, C., Palmer, P. I., and Geron, C.: Estimates of global terrestrial isoprene
 633 emissions using MEGAN (Model of Emissions of Gases and Aerosols from Nature), *Atmos. Chem. Phys.*, 6, 3181–3210,
 634 <https://doi.org/10.5194/acp-6-3181-2006>, 2006.

635 Guenther, A. B., Jiang, X., Heald, C. L., Sakulyanontvittaya, T., Duhl, T., Emmons, L. K., and Wang, X.: The Model of
 636 Emissions of Gases and Aerosols from Nature version 2.1 (MEGAN2.1): an extended and updated framework for modeling
 637 biogenic emissions, *Geosci. Model Dev.*, 5, 1471–1492, <https://doi.org/10.5194/gmd-5-1471-2012>, 2012.

638 Herman, J., Cede, A., Spinei, E., Mount, G., Tzortziou, M., and Abuhassan, N.: NO₂ column amounts from ground-based
 639 Pandora and MFDOAS spectrometers using the direct-sun DOAS technique: Intercomparisons and application to OMI
 640 validation, *J. Geophys. Res.*, 114, D13307, <https://doi.org/10.1029/2009JD011848>, 2009.

641 Herman, J., Spinei, E., Fried, A., Kim, J., Kim, J., Kim, W., Cede, A., Abuhassan, N., and Segal-Rozenhaimer, M.: NO₂ and
 642 HCHO measurements in Korea from 2012 to 2016 from Pandora spectrometer instruments compared with OMI retrievals and

with aircraft measurements during the KORUS-AQ campaign, *Atmos. Meas. Tech.*, 11, 4583–4603, <https://doi.org/10.5194/amt-11-4583-2018>, 2018.

Hong, H., Lee, H., Kim, J., Jeong, U., Ryu, J., and Lee, D.: Investigation of Simultaneous Effects of Aerosol Properties and Aerosol Peak Height on the Air Mass Factors for Space-Borne NO₂ Retrievals, *Remote Sensing*, 9, 208, <https://doi.org/10.3390/rs9030208>, 2017.

Jeong, U., and H. Hong: Assessment of tropospheric concentrations of NO₂ from the TROPOMI/Sentinel-5 Precursor for the estimation of long-term exposure to surface NO₂ over South Korea, *Remote Sensing*, 13, 1877, <https://doi.org/10.3390/rs13101877>, 2021a.

Jeong, U., and H. Hong: Comparison of total column and surface mixing ratio of carbon monoxide derived from the TROPOMI/Sentinel-5 Precursor with In-Situ measurements from extensive ground-based network over South Korea, *Remote Sensing*, 13, 3987, <https://doi.org/10.3390/rs13193987>, 2021b.

Judd, L. M., Al-Saadi, J. A., Valin, L. C., Pierce, R. B., Yang, K., Janz, S. J., Kowalewski, M. G., Szykman, J. J., Tiefengraber, M., and Mueller, M.: The Dawn of Geostationary Air Quality Monitoring: Case Studies From Seoul and Los Angeles, *Front. Environ. Sci.*, 6, 85, <https://doi.org/10.3389/fenvs.2018.00085>, 2018.

Judd, L. M., Al-Saadi, J. A., Janz, S. J., Kowalewski, M. G., Pierce, R. B., Szykman, J. J., Valin, L. C., Swap, R., Cede, A., Mueller, M., Tiefengraber, M., Abuhassan, N., and Williams, D.: Evaluating the impact of spatial resolution on tropospheric NO₂ column comparisons within urban areas using high-resolution airborne data, *Atmos. Meas. Tech.*, 12, 6091–6111, <https://doi.org/10.5194/amt-12-6091-2019>, 2019.

Judd, L. M., Al-Saadi, J. A., Szykman, J. J., Valin, L. C., Janz, S. J., Kowalewski, M. G., Eskes, H. J., Veefkind, J. P., Cede, A., Mueller, M., Gebetsberger, M., Swap, R., Pierce, R. B., Nowlan, C. R., Abad, G. G., Nehrir, A., and Williams, D.: Evaluating Sentinel-5P TROPOMI tropospheric NO₂ column densities with airborne and Pandora spectrometers near New York City and Long Island Sound, *Atmos. Meas. Tech.*, 13, 6113–6140, <https://doi.org/10.5194/amt-13-6113-2020>, 2020.

Kendrick, C. M., Koonce, P., and George, L. A.: Diurnal and seasonal variations of NO, NO₂ and PM_{2.5} mass as a function of traffic volumes alongside an urban arterial, *Atmospheric Environment*, 122, 133–141, <https://doi.org/10.1016/j.atmosenv.2015.09.019>, 2015.

Kim, D., Lee, H., Hong, H., Choi, W., Lee, Y., and Park, J.: Estimation of Surface NO₂ Volume Mixing Ratio in Four Metropolitan Cities in Korea Using Multiple Regression Models with OMI and AIRS Data, *Remote Sensing*, 9, 627, <https://doi.org/10.3390/rs9060627>, 2017.

Kim, J., Jeong, U., Ahn, M.-H., Kim, J. H., Park, R. J., Lee, H., Song, C. H., Choi, Y.-S., Lee, K.-H., Yoo, J.-M., Jeong, M.-J., Park, S. K., Lee, K.-M., Song, C.-K., Kim, S.-W., Kim, Y. J., Kim, S.-W., Kim, M., Go, S., Liu, X., Chance, K., Chan Miller, C., Al-Saadi, J., Veihelmann, B., Bhartia, P. K., Torres, O., Abad, G. G., Haffner, D. P., Ko, D. H., Lee, S. H., Woo, J.-H., Chong, H., Park, S. S., Nicks, D., Choi, W. J., Moon, K.-J., Cho, A., Yoon, J., Kim, S., Hong, H., Lee, K., Lee, H., Lee, S., Choi, M., Veefkind, P., Levelt, P. F., Edwards, D. P., Kang, M., Eo, M., Bak, J., Baek, K., Kwon, H.-A., Yang, J., Park, J., Han, K. M., Kim, B.-R., Shin, H.-W., Choi, H., Lee, E., Chong, J., Cha, Y., Koo, J.-H., Irie, H., Hayashida, S., Kasai, Y., Kanaya, Y., Liu, C., Lin, J., Crawford, J. H., Carmichael, G. R., Newchurch, M. J., Lefer, B. L., Herman, J. R., Swap, R. J., Lau, A. K. H., Kurosu, T. P., Jaross, G., Ahlers, B., Dobber, M., McElroy, C. T., and Choi, Y.: New Era of Air Quality Monitoring from Space: Geostationary Environment Monitoring Spectrometer (GEMS), 101, E1–E22, <https://doi.org/10.1175/BAMS-D-18-0013.1>, 2020.

Kley, D. and McFarland, M.: Chemiluminescence detector for NO and NO₂, *Atmos. Technol.*; (United States), 12, 1980.

Kowalewski, M. G. and Janz, S. J.: Remote sensing capabilities of the GEO-CAPE airborne simulator, *SPIE Optical Engineering + Applications*, San Diego, California, United States, 92181I, <https://doi.org/10.1117/12.2062058>, 2014.

684 Kowalewski, M.G., Janz, S., Al-Saadi, J.A., Good, W., Ruppert, L., Cole, J.: GeoTASO instrument characterization and
685 level1b radiance product generation, In: Proceedings of the 1st KORUS-AQ Science Team Meeting, Jeju, South Korea, 27
686 February–3 March 2017, 13, 2017.

687 Lamsal, L. N., Martin, R. V., Parrish, D. D., and Krotkov, N. A.: Scaling Relationship for NO₂ Pollution and Urban Population
688 Size: A Satellite Perspective, *Environ. Sci. Technol.*, 47, 7855–7861, <https://doi.org/10.1021/es400744g>, 2013.

689 Lamsal, L. N., Janz, S. J., Krotkov, N. A., Pickering, K. E., Spurr, R. J. D., Kowalewski, M. G., Loughner, C. P., Crawford, J.
690 H., Swartz, W. H., and Herman, J. R.: High-resolution NO₂ observations from the Airborne Compact Atmospheric Mapper:
691 Retrieval and validation, *J. Geophys. Res. Atmos.*, 122, 1953–1970, <https://doi.org/10.1002/2016JD025483>, 2017.

692 Latza, U., Gerdes, S., and Baur, X.: Effects of nitrogen dioxide on human health: Systematic review of experimental and
693 epidemiological studies conducted between 2002 and 2006, *International Journal of Hygiene and Environmental Health*, 212,
694 271–287, <https://doi.org/10.1016/j.ijheh.2008.06.003>, 2009.

695 Lee, K., Yu, J., Lee, S., Park, M., Hong, H., Park, S. Y., Choi, M., Kim, J., Kim, Y., Woo, J.-H., Kim, S.-W., and Song, C. H.:
696 Development of Korean Air Quality Prediction System version 1 (KAQPS v1) with focuses on practical issues, *Geosci. Model*
697 *Dev.*, 13, 1055–1073, <https://doi.org/10.5194/gmd-13-1055-2020>, 2020.

698 Leitão, J., Richter, A., Vrekoussis, M., Kokhanovsky, A., Zhang, Q. J., Beekmann, M., and Burrows, J. P.: On the improvement
699 of NO₂ satellite retrievals–aerosol impact on the air mass factors, *Atmos. Meas. Tech.*, 3, 475–493, [https://doi.org/10.5194/amt-](https://doi.org/10.5194/amt-3-475-2010)
700 3-475-2010, 2010.

701 Leitch, J. W., Delker, T., Good, W., Ruppert, L., Murcray, F., Chance, K., Liu, X., Nowlan, C., Janz, S. J., Krotkov, N. A.,
702 Pickering, K. E., Kowalewski, M., and Wang, J.: The GeoTASO airborne spectrometer project, SPIE Optical Engineering +
703 Applications, San Diego, California, United States, 92181H, <https://doi.org/10.1117/12.2063763>, 2014.

704 Levelt, P. F., van den Oord, G. H. J., Dobber, M. R., Malkki, A., Huib Visser, Johan de Vries, Stammes, P., Lundell, J. O. V.,
705 and Saari, H.: The ozone monitoring instrument, *IEEE Trans. Geosci. Remote Sensing*, 44, 1093–1101,
706 <https://doi.org/10.1109/TGRS.2006.872333>, 2006.

707 Lorente, A., Folkert Boersma, K., Yu, H., Dörner, S., Hilboll, A., Richter, A., Liu, M., Lamsal, L. N., Barkley, M., De Smedt,
708 I., Van Roozendaal, M., Wang, Y., Wagner, T., Beirle, S., Lin, J.-T., Krotkov, N., Stammes, P., Wang, P., Eskes, H. J., and
709 Krol, M.: Structural uncertainty in air mass factor calculation for NO₂ and HCHO satellite retrievals, *Atmos. Meas. Tech.*, 10,
710 759–782, <https://doi.org/10.5194/amt-10-759-2017>, 2017.

711 Ma, J. Z., Beirle, S., Jin, J. L., Shaiganfar, R., Yan, P., and Wagner, T.: Tropospheric NO₂ vertical column densities over
712 Beijing: results of the first three years of ground-based MAX-DOAS measurements (2008–2011) and satellite validation,
713 *Atmos. Chem. Phys.*, 13, 1547–1567, <https://doi.org/10.5194/acp-13-1547-2013>, 2013.

714 Malm, W. C. and Hand J. L.: An examination of the physical and optical properties of aerosols collected in the IMPROVE
715 program, *Atmospheric Environment*, 41, 3407–3427, <https://doi.org/10.1016/j.atmosenv.2006.12.012>, 2007.

716 Merlaud, A., Constantin, D., Mingireanu, F., Mocanu, I., Maes, J., Fayt, C., Voiculescu, M., Murariu, G., Georgescu, L., Van
717 Roozendaal, M.: Small whiskbroom imager for atmospheric composition monitoring (SWING) from an unmanned aerial
718 vehicle (UAV), in: Proceedings of the 21st ESA Symposium on European Rocket & Balloon Programmes and related Research,
719 Thun, Switzerland pp.9–13, 2013.

720 Meier, A. C., Schönhardt, A., Bösch, T., Richter, A., Seyler, A., Ruhtz, T., Constantin, D.-E., Shaiganfar, R., Wagner, T.,
721 Merlaud, A., Van Roozendaal, M., Belegante, L., Nicolae, D., Georgescu, L., and Burrows, J. P.: High-resolution airborne
722 imaging DOAS measurements of NO₂ above Bucharest during AROMAT, *Atmos. Meas. Tech.*, 10, 1831–1857,
723 <https://doi.org/10.5194/amt-10-1831-2017>, 2017.

724 Merlaud, A., Tack, F., Constantin, D., Georgescu, L., Maes, J., Fayt, C., Mingireanu, F., Schuettmeyer, D., Meier, A. C.,
725 Schönardt, A., Ruhtz, T., Bellegante, L., Nicolae, D., Den Hoed, M., Allaart, M., and Van Roozendaal, M.: The Small

726 Whiskbroom Imager for atmospheric composition monitoring (SWING) and its operations from an unmanned aerial vehicle
 727 (UAV) during the AROMAT campaign, *Atmos. Meas. Tech.*, 11, 551–567, <https://doi.org/10.5194/amt-11-551-2018>, 2018.

728 Nowlan, C. R., Liu, X., Leitch, J. W., Chance, K., González Abad, G., Liu, C., Zoogman, P., Cole, J., Delker, T., Good, W.,
 729 Murcray, F., Ruppert, L., Soo, D., Follette-Cook, M. B., Janz, S. J., Kowalewski, M. G., Loughner, C. P., Pickering, K. E.,
 730 Herman, J. R., Beaver, M. R., Long, R. W., Szykman, J. J., Judd, L. M., Kelley, P., Luke, W. T., Ren, X., and Al-Saadi, J. A.:
 731 Nitrogen dioxide observations from the Geostationary Trace gas and Aerosol Sensor Optimization (GeoTASO) airborne
 732 instrument: Retrieval algorithm and measurements during DISCOVER-AQ Texas 2013, *Atmos. Meas. Tech.*, 9, 2647–2668,
 733 <https://doi.org/10.5194/amt-9-2647-2016>, 2016.

734 National Institute of Environmental Research (NIER) and National Aeronautics and Space Administration (NASA): KORUS-
 735 AQ Final Science Synthesis Report, available at <https://espo.nasa.gov/sites/default/files/documents/5858211.pdf>, last access:
 736 27 June 2022, 2020.

737 Nowlan, C. R., Liu, X., Leitch, J. W., Chance, K., A., González Abad, Liu, C., Zoogman, P., Cole, J., Delker, T., Good, W.,
 738 Murcray, F., Ruppert, L., Soo, D., Follette-Cook, M. B., Janz, S. J., Kowalewski, M. G., Loughner, C. P., Pickering, K. E.,
 739 Herman, J. R., Beaver, M. R., Long, R. W., Szykman, J. J., Judd, L. M., Kelley, P., Luke, W. T., Ren, W., and Al-Saadi, J. A.:
 740 Nitrogen dioxide observations from the Geostationary Trace gas and Aerosol Sensor Optimization (GeoTASO) airborne
 741 instrument: Retrieval algorithm and measurements during DISCOVER-AQ Texas 2013, *Atmos. Meas. Tech.*, 9, 2647–2668,
 742 <http://doi.org/10.5194/atm-9-2647-2016>, 2016.

743 Nowlan, C. R., Liu, X., Janz, S. J., Kowalewski, M. G., Chance, K., Follette-Cook, M. B., Fried, A., González Abad, G.,
 744 Herman, J. R., Judd, L. M., Kwon, H.-A., Loughner, C. P., Pickering, K. E., Richter, D., Spinei, E., Walega, J., Weibring, P.,
 745 and Weinheimer, A. J.: Nitrogen dioxide and formaldehyde measurements from the GEOstationary Coastal and Air Pollution
 746 Events (GEO-CAPE) Airborne Simulator over Houston, Texas, *Atmos. Meas. Tech.*, 11, 5941–5964,
 747 <https://doi.org/10.5194/amt-11-5941-2018>, 2018.

748 Palmer, P. I., Jacob, D. J., Chance, K., Martin, R. V., Spurr, R. J. D., Kurosu, T. P., Bey, I., Yantosca, R., Fiore, A., and Li,
 749 Q.: Air mass factor formulation for spectroscopic measurements from satellites: Application to formaldehyde retrievals from
 750 the Global Ozone Monitoring Experiment, *J. Geophys. Res.*, 106, 14539–14550, <https://doi.org/10.1029/2000JD900772>, 2001.

751 Pastel, M., Pommereau, J.-P., Goutail, F., Richter, A., Pazmiño, A., Ionov, D., and Portafaix, T.: Construction of merged
 752 satellite total O₃ and NO₂ time series in the tropics for trend studies and evaluation by comparison to NDACC SAOZ
 753 measurements, *Atmos. Meas. Tech.*, 7, 3337–3354, <https://doi.org/10.5194/amt-7-3337-2014>, 2014.

754 Platt, U.: Differential absorption spectroscopy (DOAS), *Chem. Anal. Series*, 127, 27–83, 1994.

755 Platt, U., Stutz, J.: Differential absorption spectroscopy, in: *Differential Optical Absorption Spectroscopy*, Springer, Berlin,
 756 Heidelberg, pp. 135–174, 2008.

757 Popp, C., Brunner, D., Damm, A., Van Roozendaal, M., Fayt, C., and Buchmann, B.: High-resolution NO₂ remote sensing
 758 from the Airborne Prism EXperiment (APEX) imaging spectrometer, *Atmos. Meas. Tech.*, 5, 2211–2225,
 759 <https://doi.org/10.5194/amt-5-2211-2012>, 2012.

760 Prasad, A. K., Singh, R. P., and Kafatos, M.: Influence of coal-based thermal power plants on the spatial–temporal variability
 761 of tropospheric NO₂ column over India, *Environ Monit Assess*, 184, 1891–1907, <https://doi.org/10.1007/s10661-011-2087-6>,
 762 2012.

763 Qin, K., Rao, L., Xu, J., Bai, Y., Zou, J., Hao, N., Li, S., and Yu, C.: Estimating Ground Level NO₂ Concentrations over
 764 Central-Eastern China Using a Satellite-Based Geographically and Temporally Weighted Regression Model, *Remote Sensing*,
 765 9, 950, <https://doi.org/10.3390/rs9090950>, 2017.

766 Richter, A., Burrows, J. P., Nüß, H., Granier, C., and Niemeier, U.: Increase in tropospheric nitrogen dioxide over China
 767 observed from space, *Nature*, 437, 129–132, <https://doi.org/10.1038/nature04092>, 2005.

768 Rothman, L. S., Gordon, I. E., Barber, R. J., Dothe, H., Gamache, R. R., Goldman, A., Perevalov, V. I., Tashkun, S. A.,
769 Tennyson, J. HITEMP, the high-temperature molecular spectroscopic database. *Journal of Quantitative Spectroscopy and*
770 *Radiative Transfer*, 111(15), 2139–2150, 2010.

771 Schönhardt, A., Altube, P., Gerilowski, K., Krautwurst, S., Hartmann, J., Meier, A. C., Richter, A., and Burrows, J. P.: A wide
772 field-of-view imaging DOAS instrument for two-dimensional trace gas mapping from aircraft, *Atmos. Meas. Tech.*, 8, 5113–
773 5131, <https://doi.org/10.5194/amt-8-5113-2015>, 2015.

774 Shah, V., Jacob, D. J., Li, K., Silvern, R. F., Zhai, S., Liu, M., Lin, J., and Zhang, Q.: Effect of changing NO_x lifetime on the
775 seasonality and long-term trends of satellite-observed tropospheric NO₂ columns over China, *Atmos. Chem. Phys.*, 20, 1483–
776 1495, <https://doi.org/10.5194/acp-20-1483-2020>, 2020.

777 Skamarock, W., Klemp, J., Dudhia, J., Gill, D., Barker, D., Wang, W., Huang, X.-Y., and Duda, M.: A Description of the
778 Advanced Research WRF Version 3, UCAR/NCAR, <https://doi.org/10.5065/D68S4MVH>, 2008.

779 Spinei, E., Whitehill, A., Fried, A., Tiefengraber, M., Knepp, T. N., Herndon, S., Herman, J. R., Müller, M., Abuhassan, N.,
780 Cede, A., Richter, D., Walega, J., Crawford, J., Szykman, J., Valin, L., Williams, D. J., Long, R., Swap, R. J., Lee, Y., Nowak,
781 N., and Poche, B.: The first evaluation of formaldehyde column observations by improved Pandora spectrometers during the
782 KORUS-AQ field study, *Atmos. Meas. Tech.*, 11, 4943–4961, <https://doi.org/10.5194/amt-11-4943-2018>, 2018.

783 Spurr, R. and Christi, M.: On the generation of atmospheric property Jacobians from the (V)LIDORT linearized radiative
784 transfer models, *Journal of Quantitative Spectroscopy and Radiative Transfer*, 142, 109–115,
785 <https://doi.org/10.1016/j.jqsrt.2014.03.011>, 2014.

786 Tack, F., Merlaud, A., Iordache, M.-D., Danckaert, T., Yu, H., Fayt, C., Meuleman, K., Deutsch, F., Fierens, F., and Van
787 Roozendaal, M.: High-resolution mapping of the NO₂ spatial distribution over Belgian urban areas based on airborne APEX
788 remote sensing, *Atmos. Meas. Tech.*, 10, 1665–1688, <https://doi.org/10.5194/amt-10-1665-2017>, 2017.

789 Tack, F., Merlaud, A., Meier, A. C., Vlemmix, T., Ruhtz, T., Iordache, M.-D., Ge, X., van der Wal, L., Schuettmeyer, D.,
790 Ardelean, M., Calcan, A., Constantin, D., Schönhardt, A., Meuleman, K., Richter, A., and Van Roozendaal, M.:
791 Intercomparison of four airborne imaging DOAS systems for tropospheric NO₂ mapping—the AROMAPEX campaign, *Atmos.*
792 *Meas. Tech.*, 12, 211–236, <https://doi.org/10.5194/amt-12-211-2019>, 2019.

793 Tack, F., Merlaud, A., Iordache, M.-D., Pinardi, G., Dimitropoulou, E., Eskes, H., Bomans, B., Veefkind, P., and Van
794 Roozendaal, M.: Assessment of the TROPOMI tropospheric NO₂ product based on airborne APEX observations, *Atmos. Meas.*
795 *Tech.*, 14, 615–646, <https://doi.org/10.5194/amt-14-615-2021>, 2021.

796 Tzortziou, M., Parker, O., Lamb, B., Herman, J., Lamsal, L., Stauffer, R., and Abuhassan, N.: Atmospheric Trace Gas (NO₂
797 and O₃) Variability in South Korean Coastal Waters, and Implications for Remote Sensing of Coastal Ocean Color Dynamics,
798 *Remote Sensing*, 10, 1587, <https://doi.org/10.3390/rs10101587>, 2018.

799 Valks, P., Pinardi, G., Richter, A., Lambert, J.-C., Hao, N., Loyola, D., Van Roozendaal, M., and Emmadi, S.: Operational
800 total and tropospheric NO₂ column retrieval for GOME-2, *Atmos. Meas. Tech.*, 4, 1491–1514, [https://doi.org/10.5194/amt-4-](https://doi.org/10.5194/amt-4-1491-2011)
801 1491-2011, 2011.

802 Vandaele, A. C., Hermans, C., Simon, P. C., Carleer, M., Colin, R., Fally, S., Mérienne, M. F., Jenouvrier, A., and Coquart,
803 B.: Measurements of the NO₂ absorption cross-section from 42 000 cm⁻¹ to 10 000 cm⁻¹ (238–1000 nm) at 220 K and 294 K,
804 *Journal of Quantitative Spectroscopy and Radiative Transfer*, 59, 171–184, [https://doi.org/10.1016/S0022-4073\(97\)00168-4](https://doi.org/10.1016/S0022-4073(97)00168-4),
805 1998.

806 Veefkind, J. P., Aben, I., McMullan, K., Förster, H., de Vries, J., Otter, G., Claas, J., Eskes, H. J., de Haan, J. F., Kleipool, Q.,
807 van Weele, M., Hasekamp, O., Hoogeveen, R., Landgraf, J., Snel, R., Tol, P., Ingmann, P., Voors, R., Kruizinga, B., Vink, R.,
808 Visser, H., and Levelt, P. F.: TROPOMI on the ESA Sentinel-5 Precursor: A GMES mission for global observations of the
809 atmospheric composition for climate, air quality and ozone layer applications, *Remote Sensing of Environment*, 120, 70–83,
810 <https://doi.org/10.1016/j.rse.2011.09.027>, 2012.

811 Vlemmix, T., Ge, X., de Goeij, B. T. G., van der Wal, L. F., Otter, G. C. J., Stammes, P., Wang, P., Merlaud, A., Schüttemeyer,
 812 D., Meier, A. C., Veefkind, J. P., and Levelt, P. F.: Retrieval of tropospheric NO₂ columns over Berlin from high-resolution
 813 airborne observations with the spectrolite breadboard instrument, *Atmos. Meas. Tech. Discuss.*, [https://doi.org/10.5194/amt-](https://doi.org/10.5194/amt-2017-257)
 814 2017-257, in review, 2017.

815 Wiedinmyer, C., Quayle, B., Geron, C., Belote, A., McKenzie, D., Zhang, X., O'Neill, S., and Wynne, K. K.: Estimating
 816 emissions from fires in North America for air quality modeling, *Atmospheric Environment*, 40, 3419–3432,
 817 <https://doi.org/10.1016/j.atmosenv.2006.02.010>, 2006.

818 Wiedinmyer, C., Akagi, S. K., Yokelson, R. J., Emmons, L. K., Al-Saadi, J. A., Orlando, J. J., and Soja, A. J.: The Fire
 819 INventory from NCAR (FINN): a high resolution global model to estimate the emissions from open burning, *Geosci. Model*
 820 *Dev.*, 4, 625–641, <https://doi.org/10.5194/gmd-4-625-2011>, 2011.

821 Wold, S., Esbensen, K., and Geladi, P.: Principal component analysis, *Chemometrics and Intelligent Laboratory Systems*, 2,
 822 37–52, [https://doi.org/10.1016/0169-7439\(87\)80084-9](https://doi.org/10.1016/0169-7439(87)80084-9), 1987.

823 Woo, J.-H., Choi, K.-C., Kim, H. K., Baek, B. H., Jang, M., Eum, J.-H., Song, C. H., Ma, Y.-I., Sunwoo, Y., Chang, L.-S., and
 824 Yoo, S. H.: Development of an anthropogenic emission processing system for Asia using SMOKE, *Atmospheric Environment*,
 825 58, 5–13, <https://doi.org/10.1016/j.atmosenv.2011.10.042>, 2012.

826 Zoogman, P., Liu, X., Suleiman, R. M., Pennington, W. F., Flittner, D. E., Al-Saadi, J. A., Hilton, B. B., Nicks, D. K.,
 827 Newchurch, M. J., Carr, J. L., Janz, S. J., Andraschko, M. R., Arola, A., Baker, B. D., Canova, B. P., Chan Miller, C., Cohen,
 828 R. C., Davis, J. E., Dussault, M. E., Edwards, D. P., Fishman, J., Ghulam, A., González Abad, G., Grutter, M., Herman, J. R.,
 829 Houck, J., Jacob, D. J., Joiner, J., Kerridge, B. J., Kim, J., Krotkov, N. A., Lamsal, L., Li, C., Lindfors, A., Martin, R. V.,
 830 McElroy, C. T., McLinden, C., Natraj, V., Neil, D. O., Nowlan, C. R., O'Sullivan, E. J., Palmer, P. I., Pierce, R. B., Pippin, M.
 831 R., Saiz-Lopez, A., Spurr, R. J. D., Szykman, J. J., Torres, O., Veefkind, J. P., Veihelmann, B., Wang, H., Wang, J., and
 832 Chance, K.: Tropospheric emissions: Monitoring of pollution (TEMPO), *Journal of Quantitative Spectroscopy and Radiative*
 833 *Transfer*, 186, 17–39, <https://doi.org/10.1016/j.jqsrt.2016.05.008>, 2017.